

Magneto-optical properties of Group-IV–vacancy centers in diamond upon hydrostatic pressure

Meysam Mohseni,^{1,2} Lukas Razinkovas,³ Vytautas Žalandauskas,³ Gergő Thiering,¹ and Adam Gali^{1,4,5}

¹*HUN-REN Wigner Research Centre for Physics, PO. Box 49, H-1525 Budapest, Hungary*

²*Eötvös Loránd University, Pázmány Péter Sétány 1/A, H-1117 Budapest, Hungary*

³*Center for Physical Sciences and Technology (FTMC), Vilnius LT-10257, Lithuania*

⁴*Budapest University of Technology and Economics,*

Műegyetem rakpart 3., H-1111 Budapest, Hungary

⁵*MTA-WFK Lendület "Momentum" Semiconductor Nanostructures Research Group, PO. Box 49, H-1525 Budapest, Hungary*

(Dated: October 3, 2025)

In recent years, the negatively charged group-IV–vacancy defects in diamond, labeled as G4V(–) or G4V centers, have attracted significant attention in quantum information processing. In this study, we investigate the magneto-optical properties of G4V centers under high compressive hydrostatic pressures up to 180 GPa. The spin-orbit splitting of the electronic ground and excited states, as well as the hyperfine tensors, are calculated using plane-wave supercell density functional theory, providing distinctive fingerprints that uniquely characterize these defects. To this end, we develop a theory for calculating the hyperfine tensors when the electronic states are subject to the Jahn–Teller effect. We find that the zero-phonon-line energy increases with hydrostatic pressure, with the deformation potential increasing from SiV(–) to PbV(–). On the other hand, our calculated photoionization threshold energies indicate that PbV(–)-based quantum sensors can operate only up to 32 GPa, whereas SnV(–), GeV(–), and SiV(–) remain photostable up to 180 GPa. We also find that the spin-orbit splitting increases in both the electronic ground and excited states with increasing pressure. The optical transitions associated with the hyperfine fine structure of the dopant atoms are interpreted using our theoretical framework, which reproduces existing experimental data at zero strain. We show that the hyperfine levels are weakly dependent on magnetic field, and increasing pressure leads to optical transitions at longer wavelengths. Finally, we estimate the spin coherence times of the G4V centers under increasing hydrostatic pressure across different temperature regimes.

I. INTRODUCTION

The negatively charged group-IV–vacancy G4V(–) defects in diamond, commonly referred to as G4V centers, have attracted significant attention over the past decades due to their promising optical properties (see Fig. 1 for a schematic representation of their geometry and electronic structure). These color centers, including silicon-vacancy (SiV), germanium-vacancy (GeV), tin-vacancy (SnV), and lead-vacancy (PbV) defects are promising qubits for quantum communication and sensor applications [1–22]. The G4V centers have a $S = 1/2$ spin state and exhibit D_{3d} inversion symmetry [23–25], leading to outstanding optical stability compared to other color centers, such as the nitrogen-vacancy center in diamond [26, 27], which can be utilized in quantum communication technologies [20, 21]. The electronic structure of G4V centers provides an advantage in achieving coherent control of spin states using only optical methods without the need for microwave fields [28–33]. The ability of microwave-free control of spin states can be practical under extreme conditions such as high pressures, where reducing the complexity of measurement is a very important issue [18]. On the other hand, the effect of pressure on the magneto-optical properties of the G4V centers has not yet been explored in detail [18, 34], which is an inevitable step in determining the potential of these color centers in high-pressure quantum sensor applications.

In this paper, we explore the magneto-optical properties of G4V centers upon compressive hydrostatic pressure using density functional theory (DFT) plane wave supercell calculations. In particular, we focus on the fine-level structure of the electronic system, i.e., the spin-orbit and hyperfine interaction in the respective ground and excited states. These properties are intertwined with the strong electron-phonon coupling that can be described by the Jahn–Teller theory [25]. We developed a theory to accurately compute the hyperfine tensors subject to the Jahn–Teller effect. We implemented it to calculate all the critical hyperfine tensor elements of the respective group-IV dopant and the proximate ^{13}C nuclear spins. The photoionization threshold energies are also monitored in our study, along with the shift in the zero-phonon-line energy as a function of compressive hydrostatic pressure. We provide the list of pressure-dependent magneto-optical parameters that indicate the coupling strength of pressure to zero-phonon-line (ZPL) energies, spin-orbit gaps, and hyperfine levels. These parameters can be used to calibrate the actual pressure acting on the color centers. We find that the coupling strength increases when going from lighter to heavier group-IV elements in the G4V centers. Our calculations also reveal that the operation of the PbV(–) quantum sensor is limited up to 32 GPa.

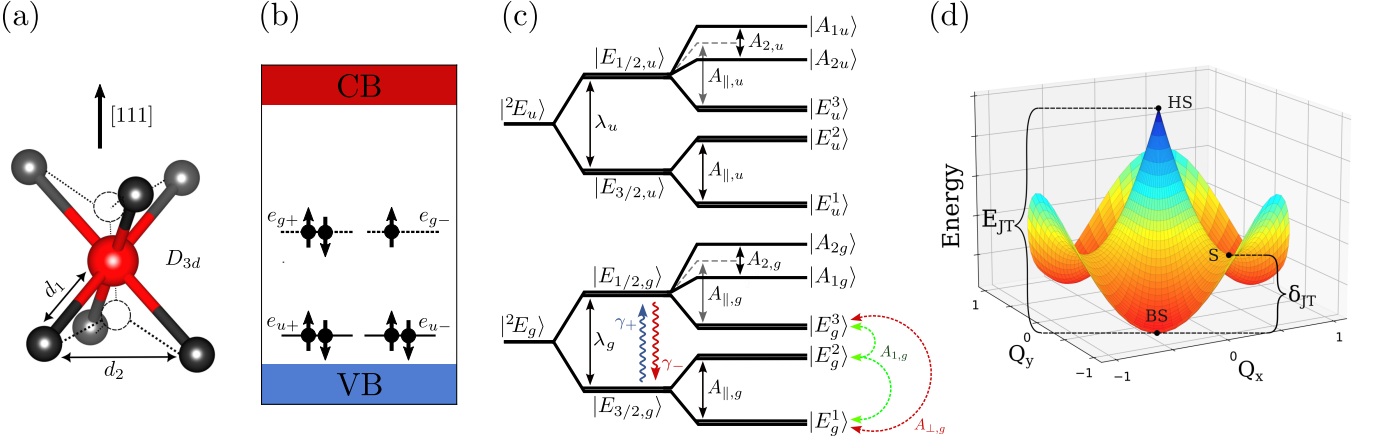


FIG. 1. Schematic diagrams illustrating the fundamental properties of G4V(−) color centers in diamond. (a) Geometry of the defect. Dashed spheres represent the two vacancies, and the interstitial dopant atom (silicon, germanium, tin, or lead) is shown as a red sphere. The critical distances under high D_{3d} symmetry are labeled as d_1 and d_2 . The dopant atom is positioned at the inversion center of the diamond. (b) Schematic single-particle defect levels in the electronic ground state (small spin-polarization splittings of $\lesssim 20$ meV omitted). The positions of the fully occupied double degenerate e_u levels and the partially occupied e_g levels vary in the various G4V(−) color centers. In the electronic excited state (not shown), the e_g levels are fully occupied, whereas a hole is left on the e_u level. (c) Electronic structure in the ground and excited states, including fine and hyperfine interactions. The hyperfine structure originates from the coupling with the impurity atom positioned at the inversion symmetry point. The fine and hyperfine states are labeled according to the double-group representations of the D_{3d} point group, following the notation in Ref. [35]. $\lambda_{g,u}$ are the effective spin-orbit splitting in the g (even parity) ground and u (odd parity) excited states. Transitions between two Kramers states occur with orbital relaxation at rates γ_{\pm} . The hyperfine coupling parameters $A_{\parallel,\{g,u\}}$ and $A_{2,\{g,u\}}$ lift the degeneracy of the fine-structure states, while $A_{\perp,\{g,u\}}$ and $A_{1,\{g,u\}}$ facilitate the mixing of spin-orbit states. (d) Adiabatic potential energy surface (APES) of the quadratic Jahn-Teller system along the ionic degrees of freedom corresponding to a single degenerate e_g -symmetry mode, described by the configuration coordinates $Q_{x,y}$. The points of BS, HS, and S represent the lowest energy broken-symmetry, the highest energy of highest symmetry and saddle point configurations, respectively. E_{JT} is the difference in energy between the high symmetry configuration and the distorted configuration. The three equivalent global minima are separated by energy barriers of δ_{JT} .

II. METHODS

We performed density functional theory (DFT) calculations [36, 37] using plane-wave supercell and the projector-augmented-wave (PAW) approach [38, 39] as implemented in the Vienna Ab-initio Simulation Package (VASP) [40, 41]. For the exchange-correlation functional, we employed the strongly constrained and appropriately normed (SCAN) meta-GGA functional [42–44], which has demonstrated accurate performance in describing structural and electronic properties of color centers in diamond [45]. For the hyperfine tensor calculations, we additionally provide results obtained using the hybrid HSE06 functional [46]. The defect structure was simulated within a $4 \times 4 \times 4$ supercell consisting of 512 atoms, with lattice constants of 14.21 Å and 14.18 Å obtained using the SCAN and hybrid functionals, respectively. Γ -point was used to sample the Brillouin zone. The structures were optimized using a convergence criterion of 10^{-2} eV/Å per atom for the Hellman-Feynman forces, with a kinetic energy cutoff of 600 eV.

The G4V(−) defects feature double-degenerate $|e_u\rangle$ and $|e_g\rangle$ localized single-particle levels, corresponding to irreducible representations of the D_{3d} symmetry group

[see Fig. 1(b)]. These levels lie within the bandgap and are occupied by seven electrons. The ground-state configuration can be described as a single-hole occupation of the $|e_g\rangle$ orbitals, giving rise to the spin-doublet 2E_g state [see Fig. 1(c)]. The excited state is formed by promoting an electron from an orbital with e_u symmetry to the $|e_g\rangle$ orbital, resulting in the 2E_u state. Geometry optimization of the electronic excited state was conducted using the Δ SCF method [47], with the Kohn–Sham orbital occupation constrained to achieve the 2E_u configuration. ZPL energies were computed as the total energy difference between the respective electronic states at their global minima on the adiabatic potential energy surfaces. The orbital degeneracy in both the ground and excited states induces Jahn–Teller coupling, which in adiabatic DFT calculations manifests as symmetry-breaking distortions along the nuclear degrees of freedom associated with the $|e_g\rangle$ symmetry [25].

Next, we address the calculation of spin-orbit coupling (SOC) and hyperfine tensors, which provide insights into the fine electronic structure of G4V(−) defects. We determined the SOC using the SCAN functional within a non-collinear framework of DFT, with the quantization axis of the spin aligned along the symmetry axis of the

defect. The SOC has a small perturbation effect on electronic states; therefore, it was calculated using the optimized high-symmetry D_{3d} configuration. After applying SOC to the system, the associated z -component of the SOC, λ_0 , splits the 2E_g and 2E_u states into two degenerate doublets. Within the hole notation, these doublets are defined as $|E_{3/2,\{g,u\}}\rangle = \{|e_{\{g,u\}+}^\uparrow\rangle, |e_{\{g,u\}-}^\downarrow\rangle\}$ and $|E_{1/2,\{g,u\}}\rangle = \{|e_{\{g,u\}-}^\uparrow\rangle, |e_{\{g,u\}+}^\downarrow\rangle\}$ [see Fig. 1(c)], where, for example, $|e_{g+}^\uparrow\rangle \equiv |e_{g+}\rangle|\uparrow\rangle$ denotes the spinor orbitals. Under the operations of the D_{3d} symmetry group, the $|e_{u\pm}\rangle$ orbitals are chosen to transform as the spherical harmonics $Y_{1,\pm 1} \sim \mp(x \pm iy)$ of the Condon-Shortley phase convention [35, 48], while the $|e_{g\pm}\rangle$ orbitals transform equivalently to angular momentum raising and lowering operators (axial vectors) $\hat{L}_\pm = \hat{L}_x \pm i\hat{L}_y$. The Hamiltonian for SOC is given by

$$\begin{aligned}\hat{H}_{\text{SOC}} &= -\lambda_{\{g,u\}}\hat{\sigma}_z\hat{S}_z \\ &= \frac{\lambda_{\{g,u\}}}{2} \left[|e_{\{g,u\}+}^\uparrow\rangle\langle e_{\{g,u\}+}^\uparrow| + |e_{\{g,u\}-}^\downarrow\rangle\langle e_{\{g,u\}-}^\downarrow| \right. \\ &\quad \left. - |e_{\{g,u\}-}^\uparrow\rangle\langle e_{\{g,u\}-}^\uparrow| - |e_{\{g,u\}+}^\downarrow\rangle\langle e_{\{g,u\}+}^\downarrow| \right], \quad (1)\end{aligned}$$

where the $\hat{\sigma}_z = \hat{L}_z$ represents the orbital angular momentum operator: $\hat{\sigma}_z|e_\pm\rangle = \pm|e_\pm\rangle$, and \hat{S}_z is the z component of the electronic spin. The negative sign of $\lambda_{\{g,u\}}$ occurs because of the hole quasiparticle. Equation 1 is obtained by projecting the atomic SOC operator into the E_g manifold of G4V centers under D_{3d} symmetry, yielding the single invariant $\lambda_{\text{SO}} L_z S_z$.

The hyperfine (HF) interaction arises from the coupling between nuclear and electron spins, contributing additional splitting in the electron spin resonance spectrum. This interaction is particularly significant when the electron spin density overlaps with the nuclear positions, providing a characteristic spectroscopic fingerprint of the atomic structure. In systems with orbital degeneracy, the HF interaction also couples to degenerate orbital components, making interaction dependent on the vibronic states of the Jahn–Teller system.

For the hyperfine interaction with the central Group-IV ion, the HF Hamiltonian is invariant under the D_{3d} double group symmetry operations. Ensuring that the HF Hamiltonian transforms as a scalar under this symmetry results in the canonical form (for a group theoretical derivation, see Appendix C):

$$\begin{aligned}\hat{H}_{\text{HF}} &= \left[\frac{1}{2} A_{\perp\{g,u\}} (\hat{S}_+ \hat{I}_- + \hat{S}_- \hat{I}_+) + 2A_{\parallel\{g,u\}} \hat{S}_z \hat{I}_z \right] \hat{\mathbb{I}} \\ &\quad - A_{1\{g,u\}} \left[(\hat{S}_z \hat{I}_+ + \hat{S}_+ \hat{I}_z) \hat{\sigma}_+ + (\hat{S}_z \hat{I}_- + \hat{S}_- \hat{I}_z) \hat{\sigma}_- \right] \\ &\quad + \frac{A_{2\{g,u\}}}{2} [\hat{S}_- \hat{I}_- \hat{\sigma}_+ + \hat{S}_+ \hat{I}_+ \hat{\sigma}_-]. \quad (2)\end{aligned}$$

Here, \hat{S}_i and \hat{I}_i denote the spin projection and spin raising or lowering operators acting on the electronic and nuclear spin degrees of freedom, respectively. The operators \mathbb{I} and $\sigma_\pm = |e_{\{g,u\}\pm}\rangle\langle e_{\{g,u\}\mp}|$ represent the identity

operator and the orbital angular momentum raising and lowering operators, respectively, acting within the two-dimensional subspace of degenerate orbitals. Here, we note that while $\hat{\sigma}_z$ is equivalent with \hat{L}_z the ladder operators $\hat{\sigma}_\pm$'s are not the same as \hat{L}_\pm . When one looks into Eq. (2) more closely angular momentum conservation appears to be violated. However, one has to take into consideration that $\hat{\sigma}_\mp$ flips the "real" angular momentum twice: $\hat{\sigma}_\mp |e_{\{g,u\}\pm}\rangle \sim \hat{L}_\mp^2 |e_{\{g,u\}\pm}\rangle \sim \hat{L}_\mp |a_{\{1g,2u\}}\rangle \sim |e_{\{g,u\}\mp}\rangle$ because one has to flip though $|a_{\{1g,2u\}}\rangle$ orbitals first. However, $|a_{\{1g,2u\}}\rangle$ lie deep in the valence band [49, 50] thus we omit \hat{L}_\pm s from discussion from now on. Finally, we note that Eq. (2) neglects the orbital hyperfine interaction, which is justified because the spin density does not build up from the atomic-like orbitals of the dopant atom.

Figure 1(c) illustrates the hyperfine energy level structure arising from the interaction with the impurity atoms in G4V defects, with the corresponding states labeled according to their irreducible representations. The hyperfine interaction splits the $E_{3/2,\{g,u\}}$ levels into two doublets of $E_{\{g,u\}}$ symmetry. In contrast, the upper $E_{1/2,\{g,u\}}$ branch is divided into a doublet of $E_{\{g,u\}}$ symmetry and two singlets of $A_{1,\{g,u\}}$ and $A_{2,\{g,u\}}$ symmetries.

The first term in Eq. (2) is isotropic with respect to the orbital degrees of freedom and remains unaffected by the ionic motion associated with the Jahn–Teller system. As such, it can be regarded as a "static" contribution to the HF interaction, unaffected by the ionic motion. Within this term, $A_{\parallel,\{g,u\}}$ induces splitting between spin-orbit-coupled (SOC) branches, while $A_{\perp,\{g,u\}}$ facilitates coupling between SOC eigenstates, as illustrated by the red dashed arrow in Fig. 1(c).

In contrast, the last two terms of Eq. (2) describe interactions that couple degenerate components of the orbital states via the $\hat{\sigma}_\pm$ operators. These contributions depend explicitly on the orbital composition and are sensitive to the vibronic state of the defect, reflecting a *dynamical* HF coupling. The parameter $A_{1,\{g,u\}}$ enables the mixing of $E_{\{g,u\}}$ states, as indicated by green dashed arrows in Fig. 1(c), while $A_{2,\{g,u\}}$ induces splitting between the $A_{1,\{g,u\}}$ and $A_{2,\{g,u\}}$ levels. In this study, we compute the values of A_1 and A_2 for the lowest vibronic state using the reduction factors proposed by Ham [51].

For a selected spin density ρ_α , the hyperfine (HF) tensor parameters can be computed using the expression:

$$\begin{aligned}A_{ij}^{(\alpha)} &= \frac{\mu_0 \hbar^2}{4\pi} \frac{\gamma_I \gamma_e}{2\langle \hat{S}_z \rangle} \int d^3r \rho_\alpha(r) \\ &\quad \times \left[\left(\frac{8\pi}{3} \delta(r) \right) + \left(\frac{3r_i r_j}{|r|^5} - \frac{\delta_{ij}}{|r|^3} \right) \right], \quad (3)\end{aligned}$$

where γ_e and γ_I are the gyromagnetic ratios of the electron and nucleus, respectively; $\rho_\alpha(r)$ is the spin density at position r , $\langle \hat{S}_z \rangle$ is the expectation value of the z component of the total electronic spin, and r_i denotes the $i = x, y, z$ components of the position vector relative to

the nucleus. The first term represents the Fermi-contact interaction, which strongly depends on the spin density localized at the nucleus, while the second term corresponds to the dipole-dipole interaction. In VASP, the HF tensor expression in Eq. (3) is modified within the projector-augmented wave (PAW) formalism [52], and the spin polarization of the core orbitals is included to ensure accurate calculation of the Fermi-contact term [53].

The HF parameters in Eq. (2) can be calculated using the real-valued representation of e -orbitals. The parameter values, derived for a coordinate system with the z -axis aligned along the symmetry axis of the D_{3d} group, are as follows [see Eq. (C3) in Appendix C and Ref. 54]:

$$\begin{aligned} A_{\parallel} &= \frac{1}{2}\mathcal{A}_{zz}^x, & A_{\perp} &= \frac{1}{2}(\mathcal{A}_{xx}^x + \mathcal{A}_{yy}^x) \\ A_1 &= q\mathcal{A}_{xz}^x, & A_2 &= q(\mathcal{A}_{yy}^x - \mathcal{A}_{xx}^x), \end{aligned} \quad (4)$$

where the subscript x indicates that the HF tensor [Eq. (3)] was computed for the hole spin density constrained to the $|e_x\rangle$ orbital of C_{3v} . The factor q represents vibronic reduction factors [51, 55], which account for the quenching of the HF interaction caused by the dynamic Jahn-Teller (DJT) effect in the ground vibronic state.

When the HF interaction involves nearby ^{13}C ions, the overall symmetry is reduced to C_{2h} , complicating the calculation of HF parameters. In Appendix D we outline the procedure for estimating the HF parameters under this reduced symmetry.

The DJT effect suppresses the orbital moment, at least partially, which is referred to as the Ham-reduction [51, 56, 57]. The inherent electronic λ_0 can be read directly from the scalar-relativistic spin-orbit splitting [58] of the respective e_g or e_u Kohn-Sham orbitals. The electronic spin-orbit splitting is suppressed due to DJT by the Ham reduction factor p ; thus, the observed value in experiments is $\lambda = p\lambda_0$. The value of p depends on the vibronic states, which we compute by explicitly incorporating the DJT effect as implemented in this study (see the derivation in Ref. 25).

In our study, we explore the Jahn-Teller effect by calculating parameters for an effective single-degenerate-mode model. This model represents motion along a symmetry-breaking direction within the e_g irreducible representation, adhering to the methodology outlined in previous works [25]. Within the linear Jahn-Teller theory, the $E_g \otimes e_g$ (electronic ground state) and $E_u \otimes e_g$ (electronic excited state) APESs have a sombrero shape. The inclusion of quadratic terms disrupts the axial symmetry, resulting in three equivalent minima and saddle points [57], as illustrated in Fig. 1(d).

Below, we discuss the *ab initio* DFT analysis of the DJT effect and the respective magneto-optical properties. To address convergence issues in degenerate high-symmetry configurations and accurately determine D_{3d} symmetry geometries, we adopt a strategy involving half-half fractional occupations in half-filled degenerate orbitals within the spin-minority channel. This method

simulates the ensemble of two degenerate states, effectively suppressing JT interactions and relaxing to the D_{3d} configuration [HS point in Fig. 1(d)]. Subsequently, shifting to integer occupations enables relaxation along the e_g -symmetry direction towards the lowest energy broken-symmetry configuration [BS point in Fig. 1(d)]. This technique enables the identification of the lowest energy point, $Q_{e_g;\text{BS}}$.

For a comprehensive examination of the APES, we parameterize $\Delta Q_{e_g;\text{BS}}$ using a parameter w . In scenarios where $w = 1$, a broken symmetry configuration emerges, whereas $w = 0$ corresponds to a high-symmetry configuration. This method allows us to systematically explore the APES for $\Delta Q_{e_g;x}$ component of an effective mode, adiabatically transitioning from $w = 1.2$ to $w = 0$ to identify minima and from $w = -1.2$ to $w = 0$ to locate saddle point, thereby mitigating convergence issues associated with degeneracy close to the high-symmetry point.

However, this technique sometimes results in divergent energies as w approaches zero from positive and negative directions due to the inability of the exchange-correlation functional to yield identical energies for degenerate densities [59]. We address this issue by applying a rigid vertical shift to one of the branches, ensuring identical energies at $w = 0$.

Assuming only linear Jahn-Teller interaction, to simplify the estimation of Jahn-Teller relaxation energy E_{JT} at different pressures and to reduce the computational complexity, we develop a novel practical computational procedure that avoids issues related to the degeneracy of electronic states. Since the slice cut of sombrero APES is described by $U(Q_{e_g;x}) = \omega^2 Q_{e_g;x}^2/2 - VQ_{e_g;x}$, where V is vibronic coupling constant, energy minimum is at $\Delta Q_{e_g;\text{BS}} = V/\omega^2$, yielding Jahn-Teller relaxation energy $E_{\text{JT}} = V^2/2\omega^2$ [57]. However, using fractional occupations described above, we suppress Jahn-Teller interactions, and the potential energy surface attains the harmonic form $U_{\text{ad}}(Q_{gx}) = \omega^2 Q_{e_g;x}^2/2$. Plugging in the coordinate of the Jahn-Teller minimum into the harmonic potential we obtain $U_{\text{ad}}(\Delta Q_{e_g;\text{BS}}) = V^2/2\omega^2 \equiv E_{\text{JT}}$. This approach allows us to estimate E_{JT} from high-symmetry and broken-symmetry geometries and one single-point calculation with fractional occupations at broken-symmetry geometry.

III. RESULTS

Throughout this study, we characterize the magneto-optical properties of the negatively charged G4V(−) color centers under compressive hydrostatic pressure. While not explicitly stated henceforth, all references to pressure will assume compressive hydrostatic conditions.

Under hydrostatic pressure, the fundamental band gap of the diamond widens, which also shifts the photoionization threshold levels of G4V defects. To account for this effect, we first compute the charge transition levels

of G4V defects to identify their photostable excitation energies, assuming single photon absorption. Then, we compute the ZPL energies under increasing hydrostatic pressure up to 180 GPa, which gives information about the fluorescence conditions for each G4V(−) color center at a given hydrostatic pressure.

After exploring charge dynamics under optical illumination, we focus on the effects of compressive hydrostatic pressure on the fine-level structure of G4V(−) centers in the electronic ground and excited states. In particular, the spin-orbit splitting is determined with hyperfine tensors for the relevant isotopes of the dopant and neighbor ^{13}C nuclear spins and the quadrupole moments of the relevant dopants in G4V(−) centers. These data serve as spectroscopic fingerprints of the G4V(−) centers under specific hydrostatic pressure conditions. Furthermore, this information is essential in understanding the temperature-dependent electron spin coherence times of G4V(−) color centers. These spin interactions are strongly interwoven with electron-phonon interaction, which we treat with Jahn–Teller theory, as briefly described in the Method section. Consequently, the Jahn–Teller parameters are calculated at each considered hydrostatic pressure for each G4V(−) color center at the electronic ground and excited states and will be reported before providing the fine-level structure.

A. Photoionization thresholds and zero-phonon line energies

The photoionization threshold energies can be calculated from the charge transition levels referenced to the appropriate band edge. In particular, the photostability of G4V(−) is of interest. In this case, the $(-|0)$ level with respect to the conduction band minimum (CBM) yields the photoionization threshold for converting the negatively charged defect to a neutral one, whereas the $(2-|-)$ level with respect to the valence band maximum (VBM) yields the photoionization threshold energy for converting the negatively charged defect to doubly negative charged one. If the ZPL energy of the G4V(−) center exceeds either of these photoionization threshold energies, the G4V(−) center cannot be considered photostable. In this case, excitation energies at or above the ZPL could induce photoionization, transferring the defect to an alternative charge state.

The charge transition levels of defects in diamond can be accurately calculated using the HSE06 functional, with an accuracy of approximately 0.1 eV [60]. Therefore, we employ this method in our study. The computational approach for determining the charge transition levels of G4V defects follows the standard procedure outlined in our previous study [25] and is based on the methodology detailed by Freysoldt *et al.* [61], which we do not reiterate here. We note that the reported values are valid at $T = 0$ K, and phonon-assisted photoionization can decrease the effective thresholds at elevated

temperatures (e.g., Ref. [62]).

We find that the increase of hydrostatic pressure from 0 to 180 GPa leads to the widening of the fundamental band gap of diamond by 0.66 eV. The calculated charge transition levels of G4V(−) shift upward with increasing pressure. The general trend is that the heavier the dopant ion, the steeper the upward shift in the charge transition level (Fig. 2). The same trend can be observed in the shift of ZPL. We already discussed its origin in our previous study for SiV(−) and GeV(−) color centers [18], which can be qualitatively explained through an investigation of Kohn–Sham molecular orbital states using a single-particle picture. In the first order, the ZPL energy scales with the difference between the unoccupied and occupied states, named e_g and e_u . Thus, the change in ZPL energy upon varying hydrostatic pressures can be estimated as $E_{\text{ZPL}}(p) \propto \varepsilon_u(p) - \varepsilon_g(p)$, where $\varepsilon_g(p)$ and $\varepsilon_u(p)$ are the Kohn–Sham energies of the orbitals $|e_g\rangle$ and $|e_u\rangle$ at pressure p , respectively. The crucial distinction among the response to hydrostatic pressures is the deformation potential of the $|e_g\rangle$ orbital, which transitions from bonding to antibonding character as the atomic number of impurity atom increases [18]. Although PbV(−) shows the most sensitive pressure dependence, this also applies to photoionization thresholds. We find that the photoionization threshold towards CBM crosses the ZPL energies around 32 GPa hydrostatic pressure, which sets a limit for PbV(−) in pressure sensor applications.

B. Dynamic Jahn–Teller effect and electron-phonon parameters

The electronic structure of both the ground and excited states of the G4V(−) centers is subject to the dynamic Jahn–Teller effect, as thoroughly characterized in Ref. 25 and subsequently utilized in further studies [14, 18, 34]. In DFT calculations, geometry optimization follows the sombrero hat potential, resulting in a low-symmetry C_{2h} geometry with the global energy minimum at zero pressure. However, the system can be constrained to retain the high-symmetry D_{3d} configuration by employing the fractional occupations described above. In D_{3d} symmetry, the distances between the three symmetrically equivalent neighbor carbon atoms are labeled by d_2 , whereas the distance between the dopant ion and the nearest neighbor carbon atoms is labeled by d_1 in Fig. 1(a), and the values are listed in Table I. The general trend is that d_1 and d_2 values increase with heavier ions in G4V(−) centers at zero pressure. Such behavior may be expected as a larger ion creates a stronger strain field around the dopant ion. For a given G4V(−) center, the d_1 and d_2 values slowly decrease with the increase of hydrostatic pressure. This response may be also expected as the hydrostatic pressure generally decrease the bond length in the diamond crystal which also holds for the bond lengths in the center of G4V defects.

For each applied hydrostatic pressure, we calculated

TABLE II. The calculated Jahn-Teller (JT) energy in meV (E_{JT}), the barrier energy in meV (δ_{JT}), the effective mode in meV ($\hbar\omega$), spin-orbit splitting λ_0 (meV), p reduction factor, g the orbital reduction factor, and λ (GHz) which is Ham reduced λ_0 for the G4V(−) defects ($\lambda = p\lambda_0$) with no applied pressure. The left/right hand side data are from SCAN/HSE06 calculations.

Defects	E_{JT} (meV)	δ_{JT} (meV)	$\hbar\omega$ (meV)	λ_0 (meV)	p	g	λ (GHz)	λ_{exp} (GHz)
Ground state								
SiV(−)	40.9 / 42.3 ^a	3.79 / 3.0 ^a	89.7 / 85.2 ^a	0.86 / 0.82 ^a	0.34 / 0.31 ^a	0.328 ^a	70.26 / 61.0 ^a	50 ^b
GeV(−)	30.6 / 30.1 ^a	4.05 / 2.0 ^a	77.0 / 82.2 ^a	2.45 / 2.20 ^a	0.38 / 0.39 ^a	0.328 ^a	222.8 / 207 ^a	181 ^c
SnV(−)	20.8 / 21.6 ^a	1.15 / 1.6 ^a	64.9 / 79.4 ^a	8.69 / 8.28 ^a	0.44 / 0.47 ^a	0.328 ^a	915.2 / 946 ^a	850 ^d
PbV(−)	15.0 / 15.6 ^a	3.88 / 0.6 ^a	52.0 / 74.9 ^a	35.0 / 34.6 ^a	0.48 / 0.54 ^a	0.328 ^a	4097 / 4514 ^a	3914 ^e
Excited state								
SiV(−)	62.6 / 78.5 ^a	1.12 / 2.7 ^a	61.0 / 73.5 ^a	8.864 / 6.96 ^a	0.133 / 0.128 ^a	0.782 ^a	286.2 / 215 ^a	260 ^b
GeV(−)	71.5 / 85.7 ^a	2.31 / 5.4 ^a	70.6 / 73.0 ^a	35.03 / 36.1 ^a	0.136 / 0.113 ^a	0.782 ^a	1155 / 987 ^a	1120 ^c
SnV(−)	67.7 / 83.1 ^a	4.20 / 6.8 ^a	68.1 / 75.6 ^a	94.77 / 96.8 ^a	0.140 / 0.125 ^a	0.782 ^a	3214 / 2897 ^a	3000 ^d
PbV(−)	87.3 / 91.6 ^a	6.69 / 12.3 ^a	77.9 / 78.6 ^a	241.4 / 245 ^a	0.116 / 0.119 ^a	0.782 ^a	6782 / 7051 ^a	-

^a Ref. 25

^b Ref. 2

^c Ref. 5

^d Ref. 7

^e Ref. 17

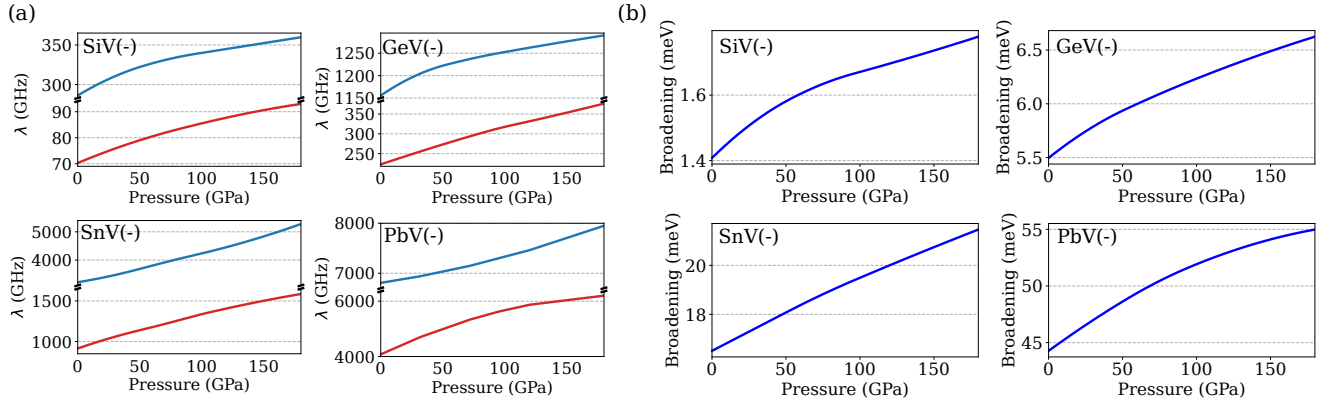


FIG. 3. Pressure dependent spin-orbit splitting as obtained with SCAN functional where the spin-orbit interaction added as perturbation to the Jahn–Teller-effect. (a) The calculated hydrostatic pressure (GPa) dependence of the effective spin-orbit splitting λ in GHz unit for G4V(−) color centers in the electronic excited and ground states plotted by blue and red lines, respectively. (b) The sum of the electronic excited and ground state's λ values associated with the zero-phonon line broadening at elevated measurement temperatures with off-resonant excitation for each G4V(−) color center as a function of the applied hydrostatic pressure.

by SCAN and HSE06 functionals, are consistent. The calculated λ values also show good agreement with experimental data for both functionals (see Table II). This result further supports the applicability of the SCAN functional for investigating the dependence of effective spin-orbit splitting on hydrostatic pressure in G4V(−) color centers.

Fig. 3(a) shows the calculated effective spin-orbit split-

ting as a function of hydrostatic pressure, obtained using SCAN functional. The general trend is that the effective spin-orbit splitting is monotonously increasing with increasing hydrostatic pressure both in the electronic ground and excited states. The calculated effective spin-orbit splitting has two factors: the Ham-reduction parameter p and the calculated electronic spin-orbit splitting λ_0 (see Table IX). We find that the Ham-reduction

parameter only slightly varies as a function of hydrostatic pressure. Therefore, the primary contribution to the overall increase in spin-orbit coupling under rising hydrostatic pressure comes from the inherent electronic spin-orbit splitting. This change can be explained by analyzing the dominant contribution to the electronic spin-orbit splitting, which arises from the spin-orbit coupling on the dopant ion [25]. As hydrostatic pressure increases, the distance (d_1) between the dopant ion and the neighbor carbon atoms decreases, enhancing the overlap of the dangling bonds with the dopant ion (see also Sec. III D). Consequently, the wavefunction cloud around the dopant ion becomes denser, contributing significantly to the spin-orbit coupling. The steepest shift in the effective spin-orbit splitting is observed for the SnV(−) color center.

In Fig. 3(b), we plot the sum of λ_g and λ_u – defined in Fig. 1(c) – as a function of the applied hydrostatic pressure, which we discuss in the context of the broadening of the ZPL emission. Off-resonant excitation of G4V(−) color centers should result in emission in all the possible combinations of states and levels depicted in Fig. 1(c). By assuming a homogeneous strain field and neglecting the isotope effects (in the GHz region), the sum of λ_g and λ_u yields the width of the zero-phonon line. In experiments, the broadening of ZPL for SiV(−) varied from 10 to 30 meV going from zero to 180 GPa of hydrostatic pressure, whereas it varied from 15 to 30 meV for GeV(−), respectively [18]. In our calculations, the spin-orbit splitting related broadening of the ZPL emission varies between 1.4 meV to 1.8 meV for SiV(−) going from zero to 180 GPa of hydrostatic pressure, whereas it varies between 5.5 meV to 6.7 meV for GeV(−), respectively. The calculated values are smaller in order of magnitude both in terms of absolute values and changes upon hydrostatic pressures. We conclude that before applying pressure to the sample, non-uniform local strain fields could be already present in the samples, which causes inhomogeneous broadening in the region of 10 meV. Applying hydrostatic pressure to the samples could further increase the variety of the local strain fields that may explain the observed wide broadening of the ZPL emission for SiV(−) and GeV(−) optical centers.

D. Hyperfine interaction

We computed the hyperfine tensors for the relevant isotopes of the dopant ion and proximate ^{13}C $I = 1/2$ nuclear spins that can be optically addressed in a resonant manner [29, 64]. The ^{13}C nuclear spins occur with a 1.1% abundance in natural diamonds. The G4V(−) color centers are often generated by ion implantation, for which the isotope can be well controlled. The non-zero nuclear spin isotopes are ^{29}Si , ^{73}Ge , ^{117}Sn , and ^{207}Pb with respective spins of $I = 1/2$, $9/2$, $1/2$, and $1/2$. For ^{73}Ge ($I = 9/2$), the nuclear quadrupole moment also contributes to the fine-level structure of the GeV(−) color

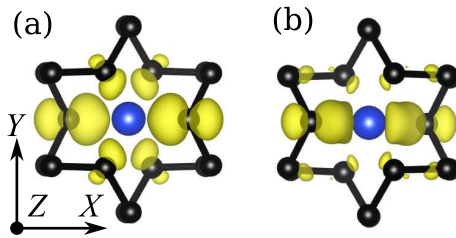


FIG. 4. The electron spin density of the SiV(−) center with low C_{2h} symmetry in the electronic (a) ground and (b) excited states depicted with the isosurface value of $5 \times 10^{-3} e/\text{\AA}$.

center, which we also consider in this section.

If these nuclear spins can be well controlled, then they could be applied as quantum memory of the system [22, 65] but may also contribute to extra spin flip-flop processes by reducing the coherence time of the electron spin of G4V(−) centers. Therefore, understanding the full hyperfine tensor and its effects on the system is important in quantum technology applications. As phonons dynamically distort the electronic states via the Jahn-Teller effect, the hyperfine and quadrupole matrix elements become modulated by the vibrational motion, which plays a vital role in spin relaxation processes [66, 67].

We note that the orbital angular momentum is significantly quenched but cannot be entirely neglected [25]. As a consequence, the remaining orbital angular momentum may contribute to the effective dipole-dipole hyperfine coupling. On the other hand, we assume that this contribution is small (e.g., a few percent), and we do not consider it further in this context.

The strong electron-phonon coupling is responsible for relatively short coherence times of the electron spin in G4V(−) defects, even at cryogenic temperatures [68]. Therefore, no electron spin resonance measurements have been reported for G4V(−) defects. The hyperfine structure can be probed optically. Resonant excitation is often performed at the $|^2E_{3/2,u}\rangle$ level, resulting in $|^2E_{3/2,u}\rangle \rightarrow |^2E_{3/2,g}\rangle$ optical transitions that appear in the zero-phonon line (ZPL) fluorescence. Because the nuclear spin state is conserved during such optical transitions, only transitions between states with the same nuclear spin projection m_I are allowed. This gives rise to transitions such as $|^2E_u^1\rangle \leftrightarrow |^2E_g^1\rangle$ and $|^2E_u^2\rangle \leftrightarrow |^2E_g^2\rangle$. [see Fig. 1(b)]. In the case of $I = 1/2$, two hyperfine-resolved lines appear in the spectrum, separated by $A_{\text{PLE}}^{\text{exp}} = A_{\parallel,u} - A_{\parallel,g}$.

In typical experimental setups, relatively weak magnetic fields in the range of 1.5–40 G are applied to lift the degeneracy of the Kramers doublets that serve as qubit states. When the magnetic field is aligned along the symmetry axis of the defect, the $|E_{\{g,u\}\pm}^i\rangle$ levels are split to first order in perturbation theory by $g\mu_B B$ [see Eqs. (C12)–(C16)], where $g \approx 2$ is the effective g -factor in both the ground and excited state manifolds, μ_B is the Bohr magneton, and B is the applied magnetic field strength. Nuclear Zeeman shifts are typically negligible

in this regime due to their much smaller magnitude.

Table III lists the calculated hyperfine parameters for dopants in G4V(−) centers. These values were obtained using the HSE06 functional to ensure accurate spin density distributions near the nuclear spins. In all investigated G4V(−) color centers, we find that the spin density around the dopant ion is lower in the electronic excited state compared to the electronic ground state, as illustrated in Figs. 4(a) and (b). This difference can be understood from symmetry considerations: the excited state wavefunction has odd (ungerade) parity, which excludes contributions from *s*-type orbitals since they do not change signs under inversion. In contrast, the ground state wavefunction has even (gerade) parity, allowing *s*-orbital contributions that enhance the Fermi-contact interaction. As a result, the static hyperfine parameters of dopant ions located at the inversion center are more significant in the ground state than in the excited state. Consequently, for dopants with non-zero nuclear spin ($I > 0$), the hyperfine splitting A_{PLE} becomes finite, enabling the optical resolution of hyperfine lines.

As shown in Table III, the dynamic hyperfine parameters are small but non-zero in both the $|^2E_u\rangle$ and $|^2E_g\rangle$ states. The parameter A_1 reflects the degree to which the spin density bends out of the *xy* plane toward the *z*-axis, while A_2 quantifies the rotational intensity of the π orbital within the *xy* plane. Both A_1 and A_2 remain small in the ground and excited states, indicating limited contribution from π orbitals and minimal out-of-plane spin density distortion [see Figs. 4(a,b)]. Nevertheless, these components of the hyperfine tensor play a role in shaping the fine structure of the spin levels in G4V(−) centers, as discussed below.

In the relevant $|^2E_{3/2,\{g,u\}}\rangle$ states split by the external magnetic field and hyperfine interaction terms $A_{\perp,\{g,u\}}$ and $A_{\parallel,\{g,u\}}$ see Eqs. (C12) and (C13) in the Appendix for details. However, in optical measurements, only the hyperfine splitting (A_{PLE}) of the photoluminescence excitation (PLE) peaks is measured that we show below

$$A_{\text{PLE}}(B) = \overbrace{A_{\parallel,g} - A_{\parallel,u}}^{A_{\text{PLE}}} \pm \left(\frac{A_{\perp,g}^2}{\lambda_g^2} - \frac{A_{\perp,u}^2}{\lambda_u^2} \right) \frac{\mu_B g_S B}{4}, \quad (5)$$

where the magnetic field aligned to the symmetry axis. We note that the magnetic field independent terms cancel out or just being negligible see Eq. (C17) for details. As a consequence, the optical transition between hyperfine lines will be weakly magnetic field dependent: there will be an extra splitting in the hyperfine peaks at large fields which is very small (~ 0.02 MHz) at $B \sim 10 \dots 50$ Gauss that were typically applied in experimental studies [34, 69].

Nevertheless, by comparing the experimental data and our theory about hyperfine-related splitting in the optical transition we find good agreement. We conclude that the hyperfine couplings are accurately calculated with our method at zero pressure. The hyperfine parameters in the ground and excited states cannot be directly ob-

served in quantum optics measurements so our data can be used for analyzing G4V(−) color centers. We provide further hyperfine data about proximate ^{13}C nuclear spins. These nuclear spins do not reside in the symmetry axis therefore the static and dynamic hyperfine tensors have to be derived for such cases that we present in Appendix D. The results are listed in Table XII.

We also studied the quadrupole moment of Ge isotope with $I = 9/2$ nuclear spin in GeV(−) for which the dynamical $Q_{1,2}$ may flip the nuclear spin as explained in Refs. [66, 67]. The quadrupole moment (Q) can be calculated as

$$Q = \frac{\rho e^2 V_{zz}}{h} \quad (6)$$

where ρ is the nuclear quadrupole moment, e is the elementary charge, V_{zz} is the electric field gradient (EFG) at the nucleus site and h is Planck's constant [70]. With using $\rho = -196 \times 10^{-31} \text{m}^2$ (Ref. 71) we obtained $Q = -13.5$ MHz, $Q_1 = -5.6$ MHz and $Q_2 = -5.0$ MHz.

As a next step, we computed the pressure dependence of the hyperfine parameters. For the sake of simplicity, we plot the absolute value of the Fermi-contact hyperfine constant for the dopants and the nearest neighbor ^{13}C nuclear spins as a function of the applied hydrostatic pressure in Figs. 5(a,b). We find that the hyperfine constants are generally decreasing with increasing hydrostatic pressures in the electronic ground state because the spin density is less localized with increasing hydrostatic pressures (see Fig. 6). We also find that the heavier the dopant the larger the change in the hyperfine constant on the dopant ion upon hydrostatic pressure. We also plot the computed A_{PLE} under hydrostatic pressure which can be directly observed in quantum optics measurements. We find that the absolute values of A_{PLE} also reduces with increasing hydrostatic pressure because the absolute value of the hyperfine constants reduces much faster in the electronic ground state than that in the electronic excited state.

E. Zeeman shift of the optical emission

Next, we investigated the effect of the constant external magnetic field on the optical emission of the G4V centers when the magnetic field is perfectly aligned with the symmetry axis of the defect. The most general microscopic theory of the spin Hamiltonian is given in Refs. [25, 72] that we do not wish to reiterate here. In this microscopic theory, the magnetic field is in part coupled to the orbital moment of the electron that is quenched by the Ham reduction factor (already defined above) and the Stevens orbital reduction factor [73] where the second one is associated with the shape of the orbital (see Ref. 25). We found earlier that the Stevens orbital reduction factor is smaller in the electronic ground state than that in the electronic excited state. We assume that the Stevens reduction parameters of the respective electronic states

TABLE III. Hyperfine parameters of the G4V(-) centers calculated using the HSE06 functional in the C_{2h} symmetry configuration. The parameters A_{\parallel} , A_{\perp} , A_1 , and A_2 are defined in Eqs. (2) and (4), and reported here as reduced values using the reduction factors listed in Table XII. The calculated A_{PLE} values correspond to the zero-field splitting observed in optical transitions between the $E_{3/2,u}$ and $E_{3/2,g}$ states (see main text for details). Experimental values $A_{\text{PLE}}^{\text{exp}}$ are taken from different studies conducted at various magnetic field strengths. Our calculations indicate that fields in the range of 10–50 G affect A_{PLE} by less than 0.15%.

Nuclear	Spin	A_1 (MHz)	A_2 (MHz)	A_{\parallel} (MHz)	A_{\perp} (MHz)	A_{PLE} (MHz)	$A_{\text{PLE}}^{\text{exp}}$ (MHz)
Ground state							
^{29}Si	1/2	-2.9	-5.9	41.7	88.7	-39.3	35 ^a
^{73}Ge	9/2	0.8	1.7	20.6	44.0	-18.4	-12.5(5) ^b
^{117}Sn	1/2	1.1	1.9	488.0	1029.7	-473.1	-484(8) ^b
^{207}Pb	1/2	-1.6	1.0	-574.7	-1192.0	565.0	-
Excited state							
^{29}Si	1/2	-0.03	-0.02	2.4	5.1	-	-
^{73}Ge	9/2	0.22	0.52	2.3	4.6	-	-
^{117}Sn	1/2	0.1	-0.43	15.0	32.3	-	-
^{207}Pb	1/2	0.06	0.77	-9.7	-20.76	-	-

^a Ref. 69

^b Ref. 34

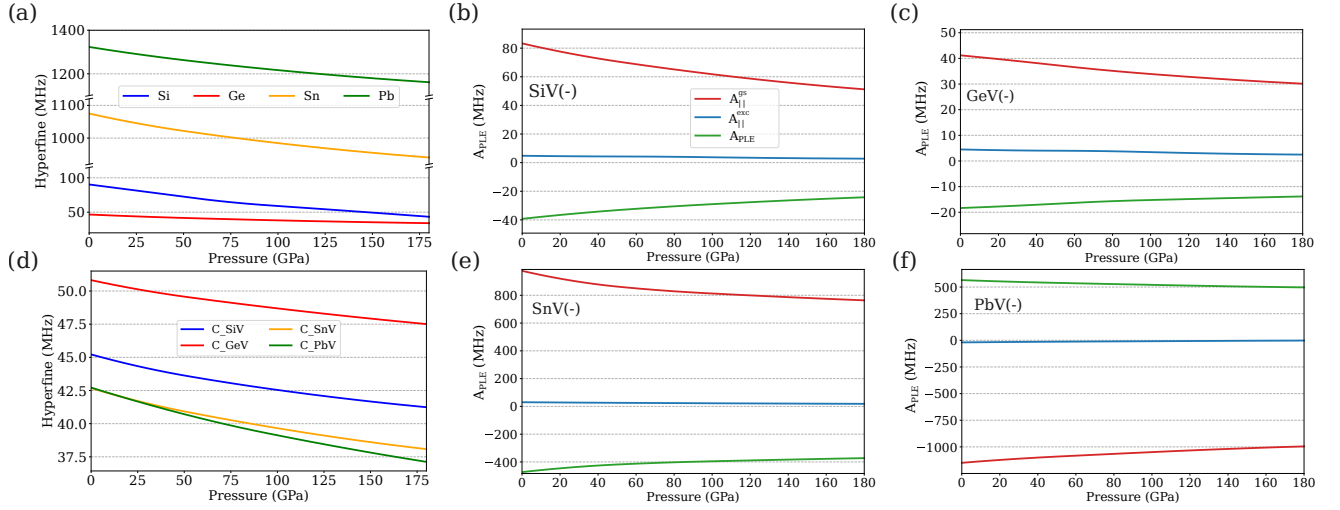


FIG. 5. Absolute value of the Fermi-contact hyperfine constants in G4V(-) centers as obtained with HSE06 functional as a function of hydrostatic pressure for (a) dopant atoms and (d) first neighbor carbon atoms. These calculations were carried out in D_{3d} symmetry configurations. The illustration of A_{PLE} , $A_{\parallel}^{\text{gs}}$ and $A_{\parallel}^{\text{exc}}$ as a function of hydrostatic pressure for dopant atoms—depicted in green, red and blue colors, respectively—(see text for details) with low C_{2h} point group symmetry for given defect centers of (b) SiV(-), (c) GeV(-), (e) SnV(-) and (f) PbV(-). The plots were fit to quadratic functions.

at zero pressure as listed in Appendix D of Ref. 25 are unaltered under hydrostatic pressures. In the simulation of Zeeman shift we go beyond the above applied theory and solve the spin-orbit and electron-phonon Hamiltonians simultaneously with the polaronic basis functions $\tilde{\Psi}_{\Gamma}$

with the spin degrees of freedom as

$$|\tilde{\Psi}_{\Gamma}\rangle = \sum_{n,m} [c_{nm}^{\chi} |e_{g\pm}\rangle |n, m\rangle |\chi\rangle + d_{nm}^{\chi} |e_{g\mp}\rangle |n, m\rangle |\chi\rangle], \quad (7)$$

where χ can be either \uparrow or \downarrow spin state. This solution represents a coupling between spins and phonons and goes *beyond* the perturbation theory of spin-orbit cou-

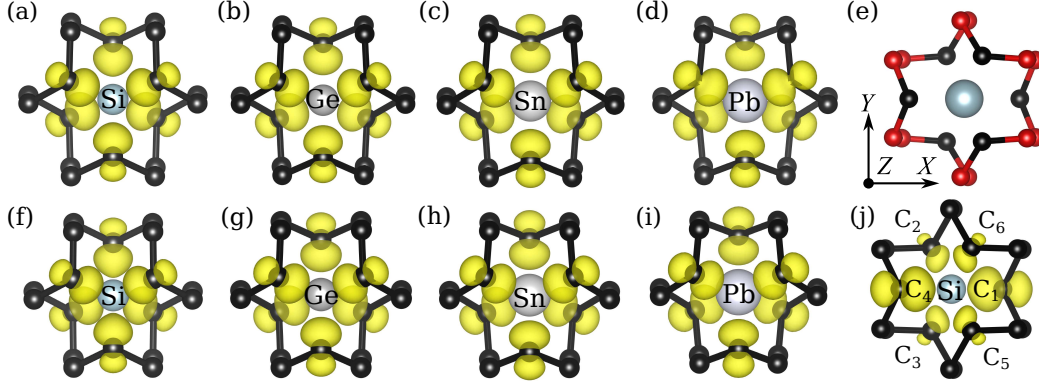


FIG. 6. Illustration of the spin density in D_{3d} symmetry. (a) SiV(-), (b) GeV(-), (c) SnV(-) and (d) PbV(-) defects with zero pressure, and (f) SiV(-), (g) GeV(-), (h) SnV(-) and (i) PbV(-) defects under 180 GPa hydrostatic pressure as obtained by HSE06 functional. (e) The positions of the first and second carbon neighbor atoms are depicted in black and red spheres, respectively. (j) The spin density of SiV(-) representative of all G4V centers in C_{2h} symmetry with no pressure. The electron spin density is depicted with an isosurface value of $5 \times 10^{-3} e/\text{\AA}$.

pling acting on the polaronic wavefunctions. Here, the subindex Γ refers to the total angular momentum of the wavefunction which is either $\frac{3}{2}$ or $\frac{1}{2}$. The parameters of the electron-phonon coupling parameters via JT-effect and the electronic spin-orbit parameter are listed in Tables II and IX.

In practical point of view, the orbital moment corrections contribute to the effective \mathbf{g} -tensor of the system that may be simply written for the ground state (g) and excited state (u) as

$$\hat{H}_{g,u}^{\text{eff}} = \lambda_{g,u} + \mu_B \mathbf{S} \mathbf{g}_{g,u} \mathbf{B}, \quad (8)$$

where μ_B is the Bohr magneton of the electron, \mathbf{B} represents the external homogeneous magnetic field. In this simplified formula, $\lambda_{g,u}$ contains all the electron-phonon related corrections whereas \mathbf{g} amalgamates all the electron-phonon related corrections and orbital moment interaction. We note that the corrections in the Zeeman term specifically occur along the symmetry axis of the defect [25, 72] that causes an observable deviation from the Bohr magneton of the free electron at 2.0023 in the Zeeman shift when the magnetic field is aligned along the symmetry axis of the defect.

With the caveat about the approximations in the microscopic theory of spin Hamiltonian, we calculated the splitting of the ZPL under magnetic fields ranging from 0 to 10 T for G4V centers under hydrostatic pressures of 0, 32, and 180 GPa where the magnetic field is perfectly aligned with the symmetry axis of the defects. We note that it is expected that the PbV(-) may not exhibit photostable optical transitions over 32 GPa but we still calculated it for the sake of complete dataset. Initially, for SiV(-) and SnV(-) centers at zero pressure, we achieved good agreement with experimental data [2, 74] which motivated us to proceed with the calculations under hydrostatic pressures. The results are plotted in Fig. 7. We considered all four possible electronic transitions from

excited E_u to the ground E_g states [2] which resulted in four distinct branches of the ZPL for each color center. The effective g-factors can be read out from the steepness of the curves. We find that the character of the Zeeman splitting under high magnetic fields is basically not altered under high pressure. This is very promising to apply these quantum sensors under extreme conditions.

F. Estimation of the electron spin coherence times

In this section, we present our estimation of the electron spin coherence times, a pivotal parameter in quantum information processing applications. We employ the phenomenological theory developed in Ref. 75, which describes the relaxation between $|E_{g\frac{3}{2}}\rangle$ and $|E_{g\frac{1}{2}}\rangle$ orbital states mediated by symmetry breaking E phonons. This model incorporates the electron-phonon coupling strength, χ , as well as the phonon density of states, ρ , to describe the underlying relaxation process. The transition between two Kramers states occur via orbital relaxation processes, characterized by the rates γ_+ and γ_- [see Fig. 1(c)]. In our theoretical framework, we incorporate the *ab initio* effective spin-orbit splitting which is essential for the estimation of the coherence times. It is important to note that although symmetry-breaking E phonons are mostly responsible for the decoherence processes, their energies are much lower than those quasi-localized E phonons that cause Jahn-Teller-effect. As a consequence, these two regimes are not intertwined; thus, it is legitimate to apply the calculated effective λ in this process and independently take the electron-phonon coupling with phonons associated with the decoherence process. Since long-wavelengths phonons responsible for decoherence cannot be directly calculated using our supercell formalism, we extract the parameters χ and ρ from experimental data that are available at zero pres-

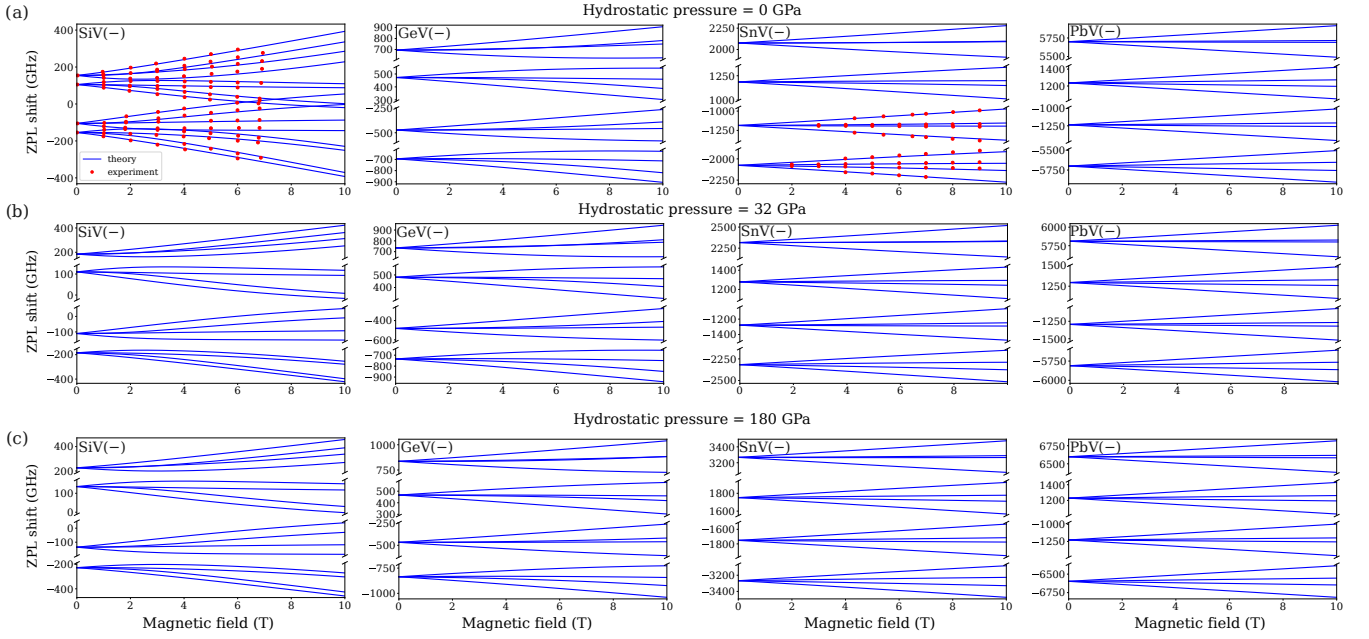


FIG. 7. The magnetic field dependency of the ZPL shift is plotted from 0 to 10 T where the magnetic field is aligned with the symmetry axis of the defect. We considered all four possible electronic transitions from excited to the ground states [2] which resulted in four distinct branches of the ZPL for each color center. We performed the calculations for three different hydrostatic pressures of (a) 0, (b) 32, and (c) 180 GPa. Nevertheless, it is expected that the PbV(−) may not exhibit photostable transitions at 180 GPa. The experimental data are depicted in red dots, while the simulated ZPL shifts are represented by blue solid lines.

sure. Furthermore we also assume that χ and ρ do not significantly change in the range of applied hydrostatic pressure. We believe that this simple approximation suffices to sketch the basic trends for the coherence times of the G4V(−) centers.

The temperature as an essential parameter of spin coherence times delineates two regions as found in Ref. 75: (i) the high-temperature region where $T \gg \frac{\hbar\lambda_g}{k_B}$ and (ii) the low-temperature region where $T \ll \frac{\hbar\lambda_g}{k_B}$. Here, \hbar and k_B are the reduced Planck and Boltzmann constants, respectively, and $\hbar\lambda_g$ is the effective spin-orbit strength in energy unit. At high temperatures, the orbital relaxation rate scales as 75

$$\gamma_+ \approx \gamma_- \approx \frac{2\pi}{\hbar} \chi \rho \lambda_g^2 k_B T, \quad (9)$$

where T denotes the temperature. In contrast, at low temperatures, the orbital relaxation rate is given by

$$\begin{aligned} \gamma_+ &\approx 2\pi \chi \rho \lambda_g^3 \exp\left(-\frac{\hbar\lambda_g}{k_B T}\right), \\ \gamma_- &\approx 2\pi \chi \rho \lambda_g^3. \end{aligned} \quad (10)$$

In this region, acoustic phonons contributing to γ_+ are exponentially suppressed, while the nonradiative relaxation process described by γ_- persists even at $T = 0$ K due to spontaneous decay (e.g., see Ref. 76).

In above equations, χ and ρ always appear together as a product. Consequently, it is unnecessary to extract

these non-calculable terms separately; instead the combination $\chi\rho$ can be considered as a single parameter. We applied the following strategy to extract this parameter from experimental data. We identify the temperature region in terms of the decoherence process at the given temperature and then we apply the respective Eq. (9) for temperature region (i) or Eq. (10) for temperature region (ii). Finally, taking the experimental coherence time $\tau = \gamma^{-1}$ of the G4V(−) center the $\chi\rho$ parameter can be extracted. In this procedure, careful choice of the experimental data is critical as the electron spin coherence time may be limited by proximate nuclear or electron spins in the system at a given temperature. However, our theory only contains the spin-phonon related decoherence, thus the experimental data should be selected from high quality samples to use spin-phonon relaxation related coherence times of G4V(−) centers.

Finally, we note that we apply the calculated effective spin-orbit parameter as obtained by SCAN functional which generally overestimate the experimental data at zero pressure (see Table II). As a consequence, the estimated coherence times are typically shorter than the experimentally observed values, reflecting the fact that larger spin-orbit splitting leads to reduced coherence times. Nevertheless, we demonstrate below that the estimated values are not far from the experimental ones, thereby, enabling a consistent characterization of the hydrostatic pressure trends using the SCAN functional dataset.

Most of the experimental data is available for SiV(−)

center at zero pressure. The $\chi\rho$ value increases by raising the temperature from 2.204×10^{-29} at $T = 0.1$ K [77] to 1.164×10^{-28} at $T = 3.6$ K [78]. In particular, the measured spin coherence time of SiV(−) with splitting of $\lambda_{\text{exp}} \approx 50$ GHz is reported by values of $\tau_{3.6\text{K}}^{\text{exp}} \approx 115$ ns [78] and $\tau_{0.1\text{K}}^{\text{exp}} \approx 13$ ms [77]. Our SCAN functional yields $\lambda = 70$ GHz which results in $\tau_{3.6\text{K}} \approx 59$ ns and $\tau_{0.1\text{K}} \approx 43$ ms, respectively, that are in the same order of magnitudes of the experimental data. We further note that two measurement temperatures will fall to different temperature regions in terms of the decoherence process: $T = 3.6$ K belongs to region (i) whereas $T = 0.1$ K belongs to region (ii). As a consequence, the pressure dependence of the estimated coherence times behaves differently at the two temperatures: $\tau_{3.6\text{K}}$ values decrease with increasing the hydrostatic pressures whereas $\tau_{0.1\text{K}}$ values increase with increasing hydrostatic pressures (Table IV).

Spin coherence time of 20 ms was reported [79] for GeV(−) with $\lambda_{\text{exp}} = 181$ GHz at $T = 300$ mK. The extracted $\chi\rho$ is 9.402×10^{-31} and it belongs to the temperature region (ii). In this case, the estimated spin coherence time increases from 49 ms (zero pressure) up to 2.63 s at hydrostatic pressure of 180 GPa (Table V).

Next, we study the coherence times of SnV(−) based on the available experimental data [12] at temperatures of 2.9 K and 6 K where $\lambda_{\text{exp}} = 850$ GHz and the decoherence process goes in the region (ii) at both temperatures. Subsequently, $\chi\rho$ is 1.175×10^{-29} at 2.9 K and 1.986×10^{-29} at 6 K. In our simulations, $\tau_{2.9\text{K}}$ values increase from 545 ns to 1.3 μs whereas $\tau_{6\text{K}}$ values decrease from 55 ns to 35 ns (Table VI).

To our knowledge, no coherence times for PbV(−) has been reported. However, it is predicted to exhibit a millisecond spin coherence time at 9 K [17] with $\lambda_{\text{exp}} = 3914$ GHz which is located in temperature region (ii). As a result, $\chi\rho = 3 \times 10^{-34}$ may be extracted. Finally, the estimated spin coherence times raised from 1.29 ms to 1.85 ms at 9 K from zero to 32 GPa hydrostatic pressures at photostable region (Table VII).

IV. SUMMARY

In this work, we studied the pressure-dependent magneto-optical spectrum of G4V centers while assuming compressive hydrostatic pressures by means of plane wave supercell density functional theory calculations. We showed that the strong electron-phonon coupling significantly modifies the electronic spin-orbit, quadrupole and hyperfine interactions. In particular, we developed a theory for calculating the effective hyperfine tensors for $E \otimes e$ Jahn-Teller systems and applied it to the G4V centers. We find that all these parameters shift with hydrostatic pressures and cross-correlation measurements of these parameters may be applied to deduce the external hydrostatic pressures. We find that the maximum pressure is set at about 32 GPa for PbV(−) cen-

TABLE IV. Hydrostatic pressure (P) dependency of spin coherence time (τ) at the given temperatures at zero to 180 GPa pressure for SiV(−) center in diamond as obtained by SCAN functional. These parameters with $T = 0.1$ K results in ($T \ll \frac{\hbar\lambda_g}{k_B}$) so Eq. 10 is applied whereas it yields ($T \gg \frac{\hbar\lambda_g}{k_B}$) with $T = 3.6$ K so Eq. 9 is applied.

P (GPa)	λ (GHz)	τ (τ_{exp}) (ms)	
		$T = 0.1\text{K}$	$T = 3.6\text{K}$
0	70	43 (13 ^a)	59 (115 ^b)
32	76	64	50
72	82	98	43
120	88	147	38
180	93	220	34

^a Ref. 78

^b Ref. 77

TABLE V. Hydrostatic pressure (P) dependency of spin coherence time (τ) at $T = 0.3$ K at zero to 180 GPa pressure for GeV(−) center in diamond as obtained by SCAN functional. These parameters results in ($T \ll \frac{\hbar\lambda_g}{k_B}$) so Eq. 10 is applied.

P (GPa)	λ (GHz)	τ (τ_{exp}) (ms)
0	223	49 (20 ^a)
32	256	106
72	294	278
120	332	762
180	376	2626

^a Ref. 79

TABLE VI. Hydrostatic pressure (P) dependency of spin coherence time (τ) at the given temperatures at zero to 180 GPa pressure for SnV(−) center in diamond as obtained by SCAN functional. These parameters with $T = 2.9$ K results in ($T \ll \frac{\hbar\lambda_g}{k_B}$) so Eq. 10 is applied whereas it yields ($T \gg \frac{\hbar\lambda_g}{k_B}$) with $T = 6$ K so Eq. 9 is applied.

P (GPa)	λ (GHz)	τ (τ_{exp}) (ns)	
		$T = 2.9\text{K}$	$T = 6\text{K}$
0	915	545 (540 ^a)	55 (59 ^a)
32	1068	608	45
72	1224	724	40
120	1407	946	37
180	1586	1291	35

^a Ref. 12

ter based pressure sensor because the photostability of PbV(−) is compromised at larger pressures. The esti-

TABLE VII. Hydrostatic pressure (P) dependency of spin coherence time (τ) at $T = 9\text{ K}$ at zero to 180 GPa pressure for PbV(−) center in diamond as obtained by SCAN functional. These parameters results in ($T \ll \frac{\hbar\lambda_d}{k_B}$) so Eq. 10 is applied.

P (GPa)	λ (GHz)	τ (τ_{exp}) (ms)
0	4436	1.29 (1.0 ^a)
32	5065	1.85
72	5744	2.87
120	6387	4.54
180	6593	5.29

^a Ref. 17

mated pressure-dependent coherence times of G4V(−) centers imply that they can be applied as quantum sensors under extreme conditions, including high constant magnetic fields when aligned with the symmetry axis of the defect centers. To put into perspective the pressure response of the G4V centers, we benchmark our computed deformation potentials against the well-characterized nitrogen-vacancy [NV(−)] center in diamond. Several experimental works have established the NV(−) center in diamond as a robust in situ pressure gauge under hydrostatic conditions. In particular, the 637 nm zero-phonon line exhibits a linear blue-shift of approximately 5.8 meV/GPa up to ~ 60 GPa [80], and the ground-state zero-field splitting D increases at ~ 14.6 MHz/GPa [81]. More recent studies have extended optical detection of magnetic resonance (ODMR) to pressures exceeding 130 GPa in improved hydrostatic-loading environments [82]. By comparison, our calculated deformation potentials for SiV(−), GeV(−), SnV(−), and PbV(−) centers are 0.54, 2.87, 2.03, and 3.94 meV/GPa, respectively [see Fig. 2(b)], confirming that inversion-symmetric group-IV vacancies couple more weakly to lattice compression than the NV(−) defect.

ACKNOWLEDGMENTS

We acknowledge the discussion with Christoph Becher and the technical help from Balázs Tóth. This work was supported by the Hungarian National Research, Development and Innovation Office (NKFIH) for Quantum Information National Laboratory of Hungary (grant no. 2022-2.1.1-NL-2022-00004), the EU QuantERA II SensExtreme project funded by NKFIH (grant no. 2019-2.1.7-ERA-NET-2022-00040) and Lithuanian Research Council (grant no. S-QUANTERA-22-1), the Horizon Europe EIC Pathfinder QuMicro project (grant no. 101046911) and the Horizon Europe Quantum Flagship SPINUS project (grant no. 101135699). G. T. was supported by the János Bolyai Research Scholarship of the Hungarian Academy of Sciences and by NKFIH grant no. START-

ING 150113.

M.M. performed the density functional theory calculations and contributed to the writing of the initial draft. L.R. and V.Ž. contributed to the dynamic Jahn–Teller and group theory analyses. G.T. developed the theoretical framework for calculating the hyperfine tensors in the presence of Jahn–Teller effects. G.T. and A.G. supervised M.M.’s computational work. A.G. wrote the initial draft and conceptualized the study. All authors contributed to the final version of the manuscript.

DATA AVAILABILITY STATEMENT

We provide additional data in the Appendices. All the other data are available from the authors upon reasonable request [83].

Appendix A: Charge transition level with associated variable dielectric constant under high compressive hydrostatic pressure

In charge transition level calculation, we used the Freysoldt-Neugebauer-Van de Walle (FNV) charge correction [84, 85] of $E_{\text{corr}} = E_{\text{el}} + q\Delta V$, where potential alignment correction ($q\Delta V$) corrects the shift in the reference potential due to the introduction of the defect in the supercell and the electrostatic correction (E_{el}) corrects the energy associated with the interaction of the defect charge with its periodic images. It considers the anisotropy of the dielectric constant and the geometry of the supercell as

$$E_{\text{el}} = \frac{q^2}{2} \left(\frac{\Delta Q}{\epsilon_0} - \frac{Q_{\text{model}}}{\epsilon} \right) \quad (\text{A1})$$

where q is the charge of the defect, ΔQ is the difference between the defect charge density and the background charge density, ϵ_0 is the vacuum permittivity, Q_{model} is the potential due to a model charge distribution, typically a Gaussian or point charge, representing the defect and ϵ is the dielectric constant.

We used the sxdefectalign code [84] to calculate charge correction as a function of hydrostatic pressure. For this purpose, it is essential to use the corresponding dielectric constant at each pressure. Therefore, we employed the VASP package to determine the dielectric constants. VASP calculates the dielectric constant using density functional perturbation theory (DFPT) and the linear response approach [86, 87]. The dielectric tensor (ϵ) is computed by considering both electronic (ϵ_{∞}) and ionic (ϵ_{ion}) as:

$$\epsilon = \epsilon_{\infty} + \epsilon_{\text{ion}}. \quad (\text{A2})$$

We listed the charge correction to the total energy and the dielectric constants (ϵ) under each hydrostatic pressure in Table VIII. We find that the charge correction to

the total energy for a given charge state is identical across all the considered defects. This consistency may be attributed to the ionic behavior of the dopants in the G4V defects, which appears to be independent of the dopant type.

TABLE VIII. The calculated hydrostatic pressure (P) dependency of the charge correction to the total energy and dielectric constant (ϵ) from zero to 180 GPa with HSE06 functional.

P (GPa)	0	32	72	120	180
ϵ	5.7	5.5	5.3	5.1	4.9
charge corrections (eV)					
G4V(± 1)	0.25	0.27	0.28	0.28	0.39
G4V(-2)	1.00	1.09	1.11	1.13	1.55

Appendix B: Additional data for the effective spin-orbit splitting

Here, we list the calculated Jahn–Teller parameters and electronic spin-orbit splitting under compressive hydrostatic pressure as obtained by SCAN functional for G4V($-$) color centers (see Table IX).

Additional data supporting this Appendix, including full input files, raw computational outputs, and extended pressure-dependent results, are available from the corresponding author upon reasonable request [?].

Appendix C: Hyperfine Hamiltonian for an orbital doublet of D_{3d} symmetry

The general form of the hyperfine (HF) tensor associated with an orbital doublet (transforming according to either the e_g or e_u irreducible representation) under D_{3d} symmetry can be systematically derived using group-theoretical methods. For hyperfine interactions involving the central group-IV ion, the HF Hamiltonian must remain invariant under all D_{3d} symmetry operations, implying that it transforms as a scalar corresponding to the A_{1g} irreducible representation. Consequently, for real-valued representations of degenerate orbitals, the perturbation introduced by the HF interaction on an orbital doublet can be expressed through a tensor convolution [55, 57]:

$$\hat{H}_{\text{HF}} = \sum_{\Gamma\gamma} \vec{S} A_{\Gamma\gamma} \vec{I} \hat{C}_{\Gamma\gamma}, \quad (\text{C1})$$

where the sum runs over the irreducible representations Γ of the D_{3d} point group. $\hat{C}_{\Gamma\gamma}$ are Clebsch–Gordan (CG) coefficient matrices determined in the orbital state space, and $A_{\Gamma\gamma}$ are the hyperfine interaction tensors that transform as row γ of the irreducible representation Γ under

the operations of the D_{3d} point group. The symmetry-allowed parameters of $A_{\Gamma\gamma}$ can be systematically obtained using group-theoretical projection operators [88].

For an orbital doublet $|e_{\{g,u\}}\rangle$ only $\hat{C}_{\Gamma\gamma}$ with “gerade” (even) symmetry is possible because orbital operators (2×2 matrices) $|e_{\{u,g\}}\rangle \otimes \langle e_{\{u,g\}}| = A_{1g} \oplus E_g \oplus A_{2g}$ built from them must be “gerade” representations. Furthermore, the interaction tensors $\hat{A}_{\Gamma\gamma}$ must be Hermitian to ensure the hyperfine energy remains real-valued and thus prevents $\hat{C}_{A_{2g}}$ to appear. Considering these constraints, the most general form of the hyperfine Hamiltonian in the real-valued representation of e -orbitals is given by

$$\begin{aligned} \hat{H}_{\text{HF}} = & \left[A_{\perp} (\hat{S}_x \hat{I}_x + \hat{S}_y \hat{I}_y) + 2A_{\parallel} \hat{S}_z \hat{I}_z \right] \hat{\mathbb{I}} \\ & + A_1 \left[\left(\hat{S}_x \hat{I}_z + \hat{S}_z \hat{I}_x \right) \hat{C}_{E_{gy}}^{(u,g)} - \left(\hat{S}_y \hat{I}_z + \hat{S}_z \hat{I}_y \right) \hat{C}_{E_{gx}}^{(u,g)} \right] \\ & + \frac{A_2}{2} \left[\left(\hat{S}_y \hat{I}_y - \hat{S}_x \hat{I}_x \right) \hat{C}_{E_{gy}}^{(u,g)} - \left(\hat{S}_x \hat{I}_y + \hat{S}_y \hat{I}_x \right) \hat{C}_{E_{gx}}^{(u,g)} \right]. \end{aligned} \quad (\text{C2})$$

Here, A_i are scalar parameters that characterize the interaction. The additional factors of 2 are introduced for convenience in subsequent analysis. The term $\hat{\mathbb{I}}$ denotes the 2×2 identity matrix for $\hat{C}_{A_{1g}}$, while $\hat{C}_{E_{gx}}$ and $\hat{C}_{E_{gy}}$ represent the CG matrices associated with the E_g irreducible representation.

In our chosen coordinate system, these matrices correspond to the standard Pauli spin matrices for the case of $|e_u\rangle$ orbitals, as $\hat{C}_{E_{gx}}^{(u)} = \hat{\sigma}_x = \begin{pmatrix} 1 & 1 \\ 1 & -1 \end{pmatrix} = |e_{u,x}\rangle \langle e_{u,y}| + |e_{u,y}\rangle \langle e_{u,x}|$ and $\hat{C}_{E_{gy}}^{(u)} = \hat{\sigma}_z = \begin{pmatrix} 1 & -1 \\ -1 & 1 \end{pmatrix} = |e_{u,x}\rangle \langle e_{u,x}| - |e_{u,y}\rangle \langle e_{u,y}|$. We note that this convention differs from that used in Ref. 55. However, we add an extra negative -1 phase for $|e_g\rangle$ by defining $\hat{C}_{E_{gx}}^{(g)} = -\hat{\sigma}_x^{(g)} = -|e_{g,x}\rangle \langle e_{g,y}| - |e_{g,y}\rangle \langle e_{g,x}|$ and $\hat{C}_{E_{gy}}^{(g)} = -\hat{\sigma}_z^{(g)} = -|e_{g,y}\rangle \langle e_{g,y}| + |e_{g,y}\rangle \langle e_{g,y}|$ for the gerade representations. We do this because the $|e_g\rangle$ state subduces into the $|e\rangle$ representation of C_{3v} differently from how the $|e_u\rangle$ state does, as we discuss in the next paragraph.

Here, we note that the subduction of the e orbitals into the C_{3v} point group should not be taken lightly. Indeed, the “ungerade” (odd) case is trivial because both $|e_{ux}\rangle$ and $|e_{uy}\rangle$ are pointing to $\{x, y\}$ Cartesian axes: $\{|e_{u,x}\rangle, |e_{u,y}\rangle\} \rightarrow \{|e_x\rangle, |e_y\rangle\}$. In simple terms, the orbitals maintain their symmetry but are relabeled without the u subscript. However, the “gerade” case is vastly different because they are transforming as axial vectors: $\{|e_{g,x}\rangle, |e_{g,y}\rangle\} \sim \{\hat{L}_x, \hat{L}_y\} = i\hbar\{z\partial_y - y\partial_z, x\partial_z - z\partial_x\} \sim \{-|e_y\rangle, +|e_x\rangle\}$, see Ref. 54 or Fig. 8(b) for visual interpretation. This has a consequence of that $\hat{\sigma}_x$ and $\hat{\sigma}_z$ invert their sign when they are discussed within C_{3v} : $\hat{\sigma}_z^{(g)} = |e_{g,x}\rangle \langle e_{g,x}| - |e_{g,y}\rangle \langle e_{g,y}| \xrightarrow{C_{3v}} |e_y\rangle \langle e_y| - |e_x\rangle \langle e_x| = -\hat{\sigma}_z$ and $\hat{\sigma}_x^{(g)} = |e_{g,x}\rangle \langle e_{g,y}| + |e_{g,y}\rangle \langle e_{g,x}| \xrightarrow{C_{3v}} -|e_x\rangle \langle e_y| - |e_y\rangle \langle e_x| = -\hat{\sigma}_x$. Simply put, one may select $|e_x\rangle$ as the orbital that remains invariant under mirror symmetry, i.e., $\hat{\sigma}_v^{(1)}|e_x\rangle = +|e_x\rangle$, and disregard the presence of inversion symmetry, as illustrated in Fig. 8. However, as

TABLE IX. The calculated ground and excited states of Jahn–Teller (JT) energy in meV (E_{JT}), the barrier energy in meV (δ_{JT}), the effective mode in meV ($\hbar\omega$), p reduction factor and λ (GHz) with SCAN functional which is Ham reduced spin-orbit splitting for the G4V(–) defects with hydrostatic pressure.

P (GPa)	Ground states					Excited states				
	E_{JT} (meV)	δ_{JT} (meV)	$\hbar\omega$ (meV)	p	λ (GHz)	E_{JT} (meV)	δ_{JT} (meV)	$\hbar\omega$ (meV)	p	λ (GHz)
SiV(–)										
0	40.86	3.79	89.70	0.34	70.26	62.58	1.12	60.81	0.133	286.21
32	39.62	3.08	88.97	0.34	76.15	58.57	1.32	59.16	0.141	311.82
72	38.47	2.97	87.68	0.35	82.12	56.69	1.6	58.08	0.144	331.62
120	38.72	2.55	88.18	0.35	87.71	56.61	1.71	58.00	0.144	344.89
180	39.58	2.24	89.43	0.35	93.01	56.42	1.78	58.08	0.145	359.72
GeV(–)										
0	30.59	4.05	77.01	0.38	222.84	71.48	2.31	70.49	0.136	1155.54
32	30.00	3.34	76.71	0.38	255.53	68.28	2.48	68.97	0.141	1204.69
72	29.18	3.34	75.59	0.38	293.72	65.70	2.65	67.95	0.146	1237.21
120	29.89	2.99	76.29	0.38	331.61	63.42	2.91	66.82	0.150	1262.39
180	30.82	2.56	78.36	0.38	376.21	62.18	3.2	67.03	0.155	1289.74
SnV(–)										
0	20.81	1.15	64.87	0.44	915.23	67.69	4.2	68.04	0.140	3214.51
32	20.47	1.10	64.94	0.44	1068.02	65.01	4.31	66.92	0.145	3490.44
72	20.58	1.09	64.54	0.44	1223.62	61.93	4.51	65.24	0.150	3938.52
120	21.17	0.36	66.08	0.44	1407.08	57.01	4.53	62.86	0.160	4456.48
180	22.08	0.29	67.54	0.43	1585.59	50.53	4.72	59.25	0.174	5275.23
PbV(–)										
0	15.02	3.88	55.98	0.48	4436.03	87.32	6.69	77.85	0.116	6782.56
32	15.12	3.98	56.43	0.48	5064.64	87.28	6.59	77.82	0.116	6973.45
72	15.27	3.90	56.13	0.48	5743.95	87.20	6.2	78.16	0.117	7170.19
120	16.49	3.89	59.04	0.47	6387.39	86.21	6.12	77.67	0.118	7417.08
180	18.27	4.43	55.94	0.46	6592.98	82.25	5.87	74.88	0.120	7964.79

noted, this $|e_x\rangle$ orbital corresponds to $|e_{g,y}\rangle$ in D_{3d} —somewhat surprisingly—and $|e_y\rangle$ corresponds to $-|e_{g,x}\rangle$. In short, we introduced the -1 sign into the CG matrices of the $|e_g\rangle$ representation to ensure that Eq. (C2) reduces to the same Hamiltonian in C_{3v} , regardless of whether we start from the $|e_u\rangle$ or the $|e_g\rangle$ case.

From this Hamiltonian, the HF parameters can be determined by calculating the HF tensor for the selected $|e_x\rangle$ orbital state as

$$\overleftarrow{S} \mathcal{A}^x \overrightarrow{I} = \begin{cases} \langle e_x | \hat{H}_{\text{HF}} | e_x \rangle & C_{3v} \text{ case} \\ \langle e_{u,x} | \hat{H}_{\text{HF}} | e_{u,x} \rangle & \text{ungerade case} \\ \langle e_{g,y} | \hat{H}_{\text{HF}} | e_{g,y} \rangle & \text{gerade case} \end{cases},$$

where \mathcal{A}^x represents the HF coupling tensor [see Eq. (3)], evaluated for the state $E_x/E_{u,x}/E_{g,y}$ in which the $|e_x\rangle/|e_{u,x}\rangle/|e_{g,y}\rangle$ orbital is occupied by a hole. From Eq. (C2), the HF tensor components are given by

$$\mathcal{A}^x = \begin{pmatrix} A_{\perp} - \frac{A_2}{2} & 0 & A_1 \\ 0 & A_{\perp} + \frac{A_2}{2} & 0 \\ A_1 & 0 & 2A_{\parallel} \end{pmatrix}, \quad (\text{C3})$$

from which one can derive Eq. (4) of the main text straightforwardly. Specifically, one can obtain the \mathcal{A}^x by *ab initio* DFT that uniquely defines all hyperfine parameters: $\mathcal{A}_{zz}^x = 2A_{\parallel}$, $\mathcal{A}_{xx}^x + \mathcal{A}_{yy}^x = 2A_{\perp}$, $\mathcal{A}_{yy}^x - \mathcal{A}_{xx}^x = A_2$, $\mathcal{A}_{xz}^x = A_1$.

In the complex electronic basis $|e_{u\pm}\rangle = \mp(|e_{u,x}\rangle \pm i|e_{u,y}\rangle)/\sqrt{2}$ and $|e_{g\pm}\rangle = (|e_{g,x}\rangle \pm i|e_{g,y}\rangle)/\sqrt{2}$, Eq. (C2) can be rewritten in canonical form as

$$\begin{aligned} \hat{H}_{\text{HF}} = & \left[\frac{1}{2} A_{\perp} (\hat{S}_+ \hat{I}_- + \hat{S}_- \hat{I}_+) + 2A_{\parallel} \hat{S}_z \hat{I}_z \right] \hat{\mathbb{I}} \\ & - A_1 \left[(\hat{S}_z \hat{I}_+ + \hat{S}_+ \hat{I}_z) \hat{\sigma}_+ + (\hat{S}_z \hat{I}_- + \hat{S}_- \hat{I}_z) \hat{\sigma}_- \right] \\ & + \frac{A_2}{2} [\hat{S}_- \hat{I}_- \hat{\sigma}_+ + \hat{S}_+ \hat{I}_+ \hat{\sigma}_-], \end{aligned} \quad (\text{C4})$$

where \hat{S}_{\pm} and \hat{I}_{\pm} represent the spin raising or lowering operators acting on the electronic and nuclear spin degrees of freedom, respectively. The operators $\hat{\sigma}_{\pm} = |e_{\{g,u\}\pm}\rangle\langle e_{\{g,u\}\mp}|$ denote the orbital angular momentum raising and lowering operators. One may notice that Eq. (C4) is the same for the three $|e\rangle/|e_u\rangle/|e_g\rangle$ cases. Both the "gerade" and "ungerade" cases are subducing into $\hat{\sigma}_{\pm}^{(u)} \xrightarrow{C_{3v}} \hat{\sigma}_{\pm} \xleftarrow{C_{3v}} \hat{\sigma}_{\pm}^{(g)}$ the same $\hat{\sigma}_{\pm}$ ladder operator

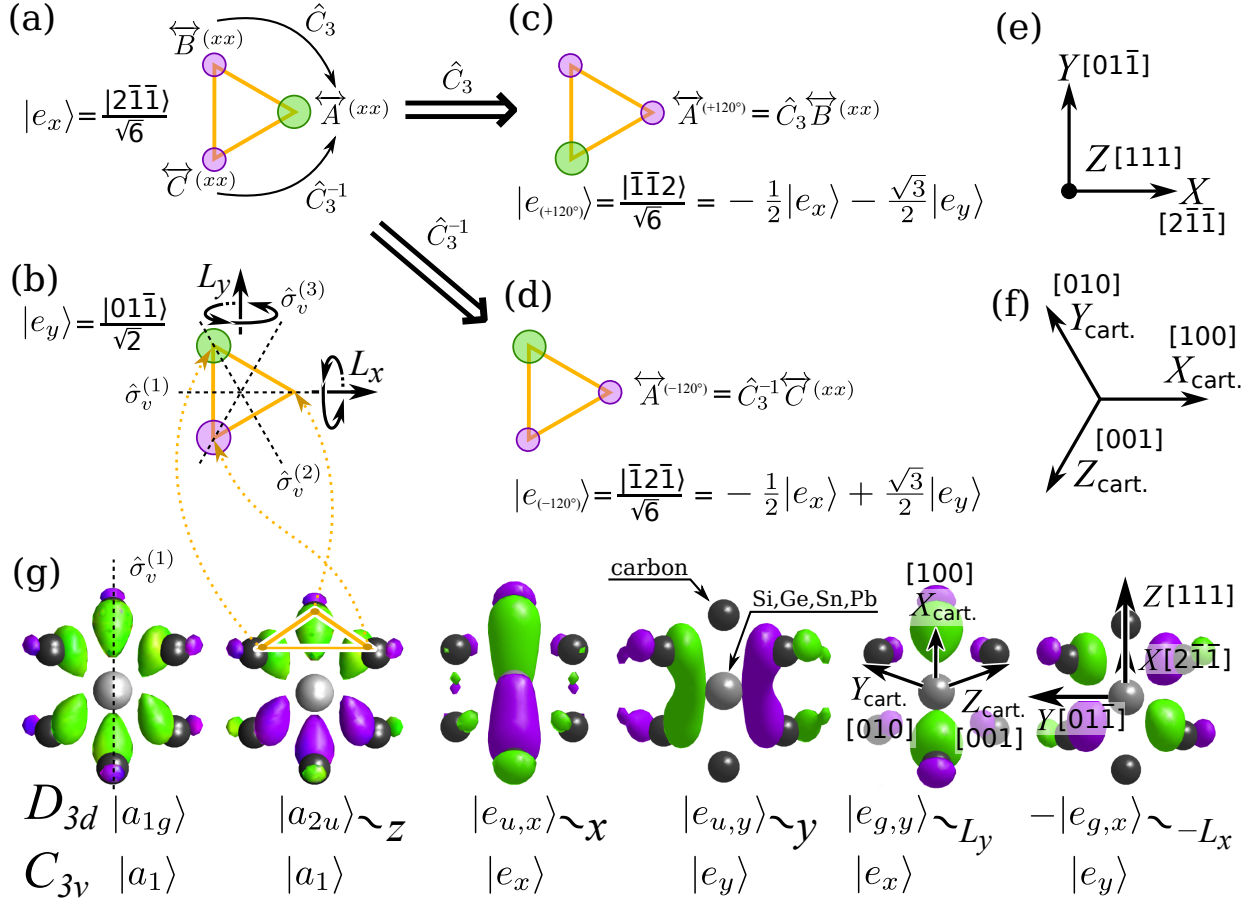


FIG. 8. Transformation of three equivalent carbon atoms. (a) and (b) represent the electronic wavefunctions when the $|e_x\rangle$ and $|e_y\rangle$ are chosen, respectively. The red and blue circles represent the positive and negative values of $|e_x\rangle$ and $|e_y\rangle$ wavefunctions, respectively that we also quantify inside the [...] parentheses. (c) and (d) depict the transformation laws for \hat{C}_3 and \hat{C}_3^{-1} rotations, respectively. (e) depicts the $z=[111]$ oriented coordinates of the G4V defects. (f) depicts the Cartesian coordinates of diamond. (g) Depiction of single particle orbitals of G4V centers. Green/purple color depicts positive/negative wavefunction phase. We also show the subduced representation labels from D_{3v} to C_{3v} .

without any additional phase unlike that was in the real valued basis. We will prove this in the next paragraph.

The "ungerade" (u) case will be $\hat{\sigma}_\pm^{(u)} = |e_{u\pm}\rangle\langle e_{u\mp}| = (-\hat{\sigma}_z^{(u)} \mp i\hat{\sigma}_x^{(u)})/2 \xrightarrow{C_{3v}} (-\hat{\sigma}_z \mp i\hat{\sigma}_x)/2 = \hat{\sigma}_\pm$. The "gerade" (g) case will be $\hat{\sigma}_\pm^{(g)} = |e_{g\pm}\rangle\langle e_{g\mp}| = (\hat{\sigma}_z^{(g)} \pm i\hat{\sigma}_x^{(g)})/2 \xrightarrow{C_{3v}} (-\hat{\sigma}_z \mp i\hat{\sigma}_x)/2 = \hat{\sigma}_\pm$. Therefore, to obtain the \mathcal{A}^x hyperfine tensor using *ab initio* DFT, one must select either the $|e_{u,x}\rangle$ or $|e_{g,y}\rangle$ orbital, as both subduce to $|e_x\rangle$ in the C_{3v} point group. However, since all of these orbitals yield the same Hamiltonian (Eq.(C4)) in the ladder operator formalism—whether in the "gerade", "ungerade", or subduced C_{3v} representation—one can directly use Eq. (4) to define the orbital-dependent A_1 and A_2 hyperfine parameters.

The solutions of Eq. (C4) can be analyzed in terms of the double group representations of the hyperfine (HF) structure. Adding the nuclear spin to the lower-lying SOC state $E_{3/2,\{g,u\}}$ [see Fig. 1] results in two doublets

of $E_{\{g,u\}}$ symmetry

$$|E_{\{g,u\}\pm}^1\rangle = \left\{ |E_{\{g,u\}+}^{\uparrow\downarrow}\rangle, -|E_{\{g,u\}-}^{\downarrow\uparrow}\rangle \right\}, \quad (\text{C5})$$

$$|E_{\{g,u\}\pm}^2\rangle = \left\{ |E_{\{g,u\}-}^{\downarrow\downarrow}\rangle, |E_{\{g,u\}+}^{\uparrow\uparrow}\rangle \right\}. \quad (\text{C6})$$

Here, for example, $|E_{g+}^{\uparrow\downarrow}\rangle$ denotes a wavefunction whose orbital part transforms as the e_{g+} irreducible representation, with the electronic spin (first arrow) in the spin-up state and the nuclear spin (second arrow) in the spin-down state.

The double group structure of the upper SOC branch results in doublet of $E_{\{g,u\}}$ symmetry and two singlets of $A_{\{1g,2u\}}$ and $A_{\{2g,1u\}}$ symmetries

$$|E_{\{g,u\}\pm}^3\rangle = \left\{ |E_{\{g,y\}+}^{\downarrow\uparrow}\rangle, -|E_{\{g,u\}-}^{\uparrow\downarrow}\rangle \right\}, \quad (\text{C7})$$

$$|A_{\{1g,2u\}}\rangle = \left(|E_{\{g,u\}-}^{\uparrow\uparrow}\rangle - |E_{\{g,u\}+}^{\downarrow\downarrow}\rangle \right) / \sqrt{2} \quad (\text{C8})$$

$$|A_{\{2g,1u\}}\rangle = \left(|E_{\{g,u\}-}^{\uparrow\uparrow}\rangle + |E_{\{g,u\}+}^{\downarrow\downarrow}\rangle \right) / \sqrt{2} \quad (\text{C9})$$

The Hamiltonian describing SOC and HF interactions in the basis $\{E_{\{g,u\}}^1, E_{\{g,u\}}^2, E_{\{g,u\}}^3, A_{\{g,u\}}, A_{2\{g,u\}}\}$ are

$$\hat{H}_{\text{SOC}} = \frac{1}{2} \begin{pmatrix} -\lambda & 0 & 0 & 0 & 0 \\ 0 & -\lambda & 0 & 0 & 0 \\ 0 & 0 & \lambda & 0 & 0 \\ 0 & 0 & 0 & \lambda & 0 \\ 0 & 0 & 0 & 0 & \lambda \end{pmatrix} \quad (\text{C10})$$

$$\hat{H}_{\text{HF}} = \frac{1}{2} \begin{pmatrix} -A_{\parallel} & A_1 & A_{\perp} & 0 & 0 \\ A_1 & A_{\parallel} & A_1 & 0 & 0 \\ A_{\perp} & A_1 & -A_{\parallel} & 0 & 0 \\ 0 & 0 & 0 & A_{\parallel} - A_2 & 0 \\ 0 & 0 & 0 & 0 & A_{\parallel} + A_2 \end{pmatrix} \quad (\text{C11})$$

Neglecting Zeeman interactions other than those arising from the coupling of the magnetic field with the electron spin, and assuming the magnetic field is aligned along the symmetry axis of the defect, the Zeeman interaction is expressed as $\hat{H}_Z = \mu_B g_S \hat{S}_z B$. Here, $g_S \approx 2$, μ_B represents the effective g -factor of the electron and the Bohr magneton, respectively, and B is the strength of the applied magnetic field. This interaction splits the E_g doublets by an energy of $g_S \mu_B B$ and also induces mixing between the $A_{\{1g,2u\}}$ and $A_{\{2g,1u\}}$ states.

Using the states described above as the zeroth-order basis, the fine-structure energies of these states—up to second-order perturbation theory—are given by

$$E[E_{\{g,u\}}^1] = \frac{1}{2}(-\lambda - A_{\parallel} \pm \mu_B g_S B) - \frac{1}{4} \left[\frac{A_1^2}{A_{\parallel} \mp \mu_B g_S B} + \frac{A_{\perp}^2}{\lambda \mp \mu_B g_S B} \right] \quad (\text{C12})$$

$$E[E_{\{g,u\}}^2] = \frac{1}{2}(-\lambda + A_{\parallel} \mp \mu_B g_S B) + \frac{1}{4} A_1^2 \left[\frac{1}{A_{\parallel} \mp \mu_B g_S B} - \frac{1}{\lambda - A_{\parallel}} \right] \quad (\text{C13})$$

$$E[E_{\{g,u\}}^3] = \frac{1}{2}(\lambda - A_{\parallel} \mp \mu_B g_S B) + \frac{1}{4} \left[\frac{A_{\perp}^2}{\lambda \mp \mu_B g_S B} + \frac{A_1^2}{\lambda - A_{\parallel}} \right] \quad (\text{C14})$$

$$E[A_{\{1g,2u\}}] = \frac{1}{2}(\lambda + A_{\parallel} - A_2) - \frac{(\mu_B g_S B)^2}{4A_2} \quad (\text{C15})$$

$$E[A_{\{2g,1u\}}] = \frac{1}{2}(\lambda + A_{\parallel} + A_2) + \frac{(\mu_B g_S B)^2}{4A_2}, \quad (\text{C16})$$

where we omit the g, u subscripts on $A_1, A_2, A_{\parallel}, A_{\perp}$, and λ on the right-hand side of the equations for simplicity.

In experiments, one can measure the difference between the PLE signals: $A_{\text{PLE}} = (E[E_{u\pm}^1] - E[E_{g\pm}^1]) - (E[E_{u\pm}^2] - E[E_{g\pm}^2])$. Thus, the leading terms in approximation of $A_1, A_{\perp}, A_{\parallel} \ll \mu_B g_S B \ll \lambda$ will be

$$A_{\text{PLE}}(B) \approx \overbrace{A_{\parallel,u} - A_{\parallel,g}}^{A_{\text{PLE}}} + \frac{A_{\perp,g}^2}{4\lambda_g} - \frac{A_{\perp,u}^2}{4\lambda_u} \pm \left(\frac{A_{\perp,g}^2}{\lambda_g^2} - \frac{A_{\perp,u}^2}{\lambda_u^2} \right) \frac{\mu_B g_S B}{4}, \quad (\text{C17})$$

on which we note that the magnetic field independent correction is negligible to A_{PLE} thus we omit it from Eq. (5) of the main text.

We note that one can reach avoided crossing by setting the external magnetic field as $A_{\parallel,g} \approx \mu_B g_S B$. In this case the effect of $A_{1,g} \approx 1 \dots 3$ MHz on the PLE spectrum will be observable, in principle, because $A_{1,u} \approx 0$ MHz, according to our calculations (see Table III). This can be readily derived where Eqs. (C12) - (C16) become invalid and Eqs. (C10) - (C11) should be directly diagonalized at the avoided crossing condition. However, the observation at this condition (low magnetic fields) could be very difficult, thus we omit this discussion in the main text.

Appendix D: Hyperfine interaction for ^{13}C neighbors

In the previous Appendix C we discussed thoroughly the case of the central atom. However, we need a more generic form for ^{13}C because they are not sitting on the central high symmetry point that of D_{3d} . As before, hyperfine tensor elements can be evaluated by spin-polarized DFT whenever the $|e_x\rangle$ or $|e_y\rangle$ orbital is being occupied for defects exhibiting D_{3d} symmetry. In simple words, hyperfine tensor elements can be evaluated whenever the $|e_x\rangle$ or $|e_y\rangle$ state is selected. Therefore, the hyperfine interaction depicted can be extended for orbital degrees of freedom as

$$\hat{H}_{\text{HF}}^{13\text{C}} = \overleftrightarrow{S} \overleftrightarrow{A}^{(xx)} \overrightarrow{I} |e_x\rangle \langle e_x| + \overleftrightarrow{S} \overleftrightarrow{A}^{(xy)} \overrightarrow{I} |e_x\rangle \langle e_y| + \overleftrightarrow{S} \overleftrightarrow{A}^{(yx)} \overrightarrow{I} |e_y\rangle \langle e_x| + \overleftrightarrow{S} \overleftrightarrow{A}^{(yy)} \overrightarrow{I} |e_y\rangle \langle e_y|, \quad (\text{D1})$$

where $\overleftrightarrow{A}^{(xx)}|_{ij} = \mathcal{A}_{ij}^x$ and $\overleftrightarrow{A}^{(yy)}|_{ij} = \mathcal{A}_{ij}^y$ tensors can be determined by applying Eq. (3) upon spin densities of $|e_x\rangle$ and $|e_y\rangle$, respectively. However, $\overleftrightarrow{A}^{(xy)}$, $\overleftrightarrow{A}^{(yx)}$ off-diagonal terms cannot be computed directly. We also cannot act similarly to what we did in Eq. (C2) because ^{13}C ions are not sitting in the central position.

First, we introduce Pauli matrices ($\hat{\sigma}_x = \begin{pmatrix} 1 & 1 \\ 1 & -1 \end{pmatrix} = |e_x\rangle \langle e_y| + |e_y\rangle \langle e_x|$, $\hat{\sigma}_y = \begin{pmatrix} -i & 1 \\ 1 & i \end{pmatrix}$, $\hat{\sigma}_z = \begin{pmatrix} 1 & 0 \\ 0 & -1 \end{pmatrix} = |e_x\rangle \langle e_x| - |e_y\rangle \langle e_y|$) for orbital degrees of freedom and thus Eq. (D1) can be transformed into a compact form as

$$\hat{H}_{\text{HF}}^{13\text{C}} = \overleftrightarrow{S} \overleftrightarrow{A} \overrightarrow{I} + \overleftrightarrow{S} \overleftrightarrow{A}_x \overrightarrow{I} \hat{\sigma}_z + \overleftrightarrow{S} \overleftrightarrow{A}_y \overrightarrow{I} \hat{\sigma}_x + \underbrace{\overleftrightarrow{S} \overleftrightarrow{A}_z \overrightarrow{I} i \hat{\sigma}_y}_{=0} \quad (\text{D2})$$

by introducing the following hyperfine tensors as

$$\overleftrightarrow{A} = \frac{1}{2} \left(\overleftrightarrow{A}^{(xx)} + \overleftrightarrow{A}^{(yy)} \right) \quad (\text{D3a})$$

$$\overleftrightarrow{A}_x = \frac{1}{2} \left(\overleftrightarrow{A}^{(xx)} - \overleftrightarrow{A}^{(yy)} \right) \quad (\text{D3b})$$

$$\overleftrightarrow{A}_y = \frac{1}{2} \left(\overleftrightarrow{A}^{(xy)} + \overleftrightarrow{A}^{(yx)} \right) \quad (\text{D3c})$$

$$\overleftrightarrow{A}_z = \frac{1}{2} \left(\overleftrightarrow{A}^{(xy)} - \overleftrightarrow{A}^{(yx)} \right) = 0, \quad (\text{D3d})$$

where \overleftrightarrow{A}_z is zero because hyperfine interaction is real-valued thus symmetric.

TABLE X. The raw data of hyperfine tensors in both D_{3d} and C_{2h} symmetries for G4V(−) defects at zero pressure as obtained in HSE06 calculations in the electronic ground state. A_{xx} , A_{yy} and A_{zz} are the symmetric hyperfine tensor elements. A_{xy} , A_{xz} and A_{yz} parameters are the asymmetric hyperfine tensor elements. The unitless reduction factor q is given for each defect associated with the Jahn–Teller effect. Atoms are labeled for low C_{2h} symmetry configuration in Fig. 6(j) and the spin density of high D_{3d} symmetry configuration is illustrated in Fig. 6.

Defect	q	A_{xx} (MHz)	A_{yy} (MHz)	A_{zz} (MHz)	A_{xy} (MHz)	A_{xz} (MHz)	A_{yz} (MHz)
SiV(−)	0.67						
C_{2h}							
C _{2,3,5,6}		18.36	22.91	21.14	6.03	−5.17	−7.53
C _{1,4}		98.46	100.94	98.45	−28.79	28.26	−28.79
²⁹ Si		87.08	85.48	87.09	−4.27	3.15	−4.25
D_{3d}							
C-first neighbor		44.85	44.85	45.95	13.02	−13.41	−13.41
C-second neighbor		−2.60	−1.87	−3.32	−1.60	0.03	0.47
²⁹ Si		90.29	90.29	90.29	−1.70	−1.70	−1.70
GeV(−)	0.69						
C_{2h}							
C _{2,3,5,6}		19.76	23.84	22.14	6.69	−5.83	−7.92
C _{1,4}		113.87	112.83	81.39	−31.78	31.75	−31.79
⁷³ Ge		43.24	42.84	43.24	−1.63	0.45	−1.64
D_{3d}							
C-first neighbor		50.64	50.64	51.17	14.74	−14.87	−14.87
C-second neighbor		−3.91	−4.30	−3.13	0.11	−1.22	0.51
⁷³ Ge		46.61	46.61	46.61	−0.93	−0.93	−0.93
SnV(−)	0.72						
C_{2h}							
C _{2,3,5,6}		16.32	20.34	18.48	7.13	−6.23	−8.33
C _{1,4}		95.15	95.64	95.16	−32.49	32.50	−32.49
¹¹⁷ Sn		1012.14	1011.20	1012.15	−18.766	−16.214	−18.763
D_{3d}							
C-first neighbor		42.61	42.61	42.84	15.40	−15.50	−15.50
C-second neighbor		−9.59	−9.85	−9.59	0.05	0.97	0.05
¹¹⁷ Sn		1074.989	1074.985	1074.99	−18.066	−18.066	−18.062
PbV(−)	0.74						
C_{2h}							
C _{2,3,5,6}		14.83	18.50	16.65	7.15	−6.23	−8.20
C _{1,4}		99.96	99.02	99.96	−33.97	34.53	−33.97
²⁰⁷ Pb		−1179.04	−1175.31	−1179.05	14.46	13.63	14.45
D_{3d}							
C-first neighbor		42.83	42.83	42.51	16.21	−16.08	−16.08
C-second neighbor		−12.13	−10.79	−11.97	0.30	−0.06	−1.26
²⁰⁷ Pb		−1323.24	−1323.24	−1323.24	14.27	14.27	14.27

Next, we discuss how to calculate these hyperfine interactions in practice within spin-polarized DFT calculations. In the usual Born-Oppenheimer *ab initio* DFT calculations, the double degenerate $|e_{\{g,u\}}\rangle$ orbital is occupied by a single electron in the ground state for G4V(−) defect. We analyze the system by assuming that $|e_{\{g,u\}(x)}\rangle$ is occupied by an electron in the symmetry configuration D_{3d} . Among the six equivalent immediate carbon neighbor atoms together with inversion symmetry, two pairs of three carbon atoms can be rotated to

each other about the C_3 symmetry axis (see Fig. 8), e.g., C₁, C₂, C₃ carbon atoms exhibit $\overleftrightarrow{A}^{(xx)}$, $\overleftrightarrow{B}^{(xx)}$, $\overleftrightarrow{C}^{(xx)}$ hyperfine tensors, respectively. In this example, we define the following hyperfine matrices for C₁,

$$\overleftrightarrow{A}^{(xx)} = \overleftrightarrow{A}^{(0^\circ)} = \langle +1; 0 | \hat{H}_{\text{HF}}^{13\text{C}} | +1; 0 \rangle = \overleftrightarrow{A} + \overleftrightarrow{A}_x, \quad (\text{D4})$$

where $\langle +1; 0 |$ and $| +1; 0 \rangle$ indicate being fully in $|e_x\rangle$ orbital than $|e_y\rangle$, with using the notation of $| +1, 0 \rangle = |e_x\rangle$ and $| 0, +1 \rangle = |e_y\rangle$.

TABLE XI. The raw data of hyperfine tensors in both D_{3d} and C_{2h} symmetries for G4V(−) defects at zero pressure as obtained in HSE06 calculations in the electronic excited state. A_{xx} , A_{yy} and A_{zz} are the symmetric hyperfine tensor elements. A_{xy} , A_{xz} and A_{yz} parameters are the asymmetric hyperfine tensor elements. The reduction factor q is given for each defect associated with the Jahn–Teller effect. Atoms are labeled for low C_{2h} symmetry configuration in Fig. 6(j) and the spin density of high D_{3d} symmetry configuration is illustrated in Fig. 6.

Defect	q	A_{xx} (MHz)	A_{yy} (MHz)	A_{zz} (MHz)	A_{xy} (MHz)	A_{xz} (MHz)	A_{yz} (MHz)
SiV(−)							
C_{2h}							
$C_{1,4}$		40.72	37.07	36.95	22.24	22.32	53.44
$C_{2,3,5,6}$		21.48	14.03	14.38	13.83	14.45	17.54
^{29}Si	0.57	4.97	5.02	4.96	4.91	4.86	4.90
D_{3d}							
C-first neighbor		−16.09	−16.09	−20.87	−14.94	−17.57	−17.57
^{29}Si		36.21	36.21	36.21	36.19	36.19	36.19
GeV(−)	0.57						
C_{2h}							
$C_{1,4}$		−8.57	−8.57	−9.73	−10.30	−8.50	−8.50
$C_{2,3,5,6}$		5.39	3.91	−1.21	−10.82	13.54	−6.84
^{73}Ge		4.59	4.51	4.59	4.28	5.01	4.28
D_{3d}							
C-first neighbor		2.91	2.91	2.42	3.01	2.44	2.44
^{73}Ge		15.437	15.912	15.439	−0.507	−0.165	−0.508
SnV(−)							
C_{2h}							
$C_{1,4}$		122.80	123.52	122.78	89.45	156.41	89.46
$C_{2,3,5,6}$		24.32	25.96	21.86	16.12	18.35	30.55
^{117}Sn	0.57	31.523	30.845	31.5	30.596	30.347	30.559
D_{3d}							
C-first neighbor		13.183	12.892	14.026	9.292	−9.237	−9.067
^{117}Sn		183.785	211.081	−22.512	−60.844	146.023	121.711
PbV(−)	0.56						
C_{2h}							
$C_{1,4}$		53.72	55.04	53.72	32.67	75.57	32.67
$C_{2,3,5,6}$		13.07	12.16	11.31	9.06	14.71	9.97
^{207}Pb		−18.15	−18.11	−18.68	−18.37	−17.57	−17.65
D_{3d}							
C-first neighbor		19.86	19.86	20.76	27.81	12.19	12.19
^{207}Pb		−793.26	−793.26	−793.26	−1004.34	−1004.34	−1004.34

The hyperfine tensors of C_2 and C_3 can be rotated to that of C_1 by $\pm 120^\circ$ rotations as

$$\begin{aligned}\hat{C}_3 \overleftrightarrow{B}^{(xx)} &= \overleftrightarrow{A}^{(+120^\circ)} = \left\langle -\frac{1}{2}; -\frac{\sqrt{3}}{2} \left| \hat{H}_{\text{HF}}^{13\text{C}} \right| -\frac{1}{2}; -\frac{\sqrt{3}}{2} \right\rangle \\ &= \overleftrightarrow{A} - \frac{1}{2} \overleftrightarrow{A}_x + \frac{\sqrt{3}}{2} \overleftrightarrow{A}_y,\end{aligned}\quad (\text{D5a})$$

$$\begin{aligned}\hat{C}_3^{-1} \overleftrightarrow{C}^{(xx)} &= \overleftrightarrow{A}^{(-120^\circ)} = \left\langle -\frac{1}{2}; +\frac{\sqrt{3}}{2} \left| \hat{H}_{\text{HF}}^{13\text{C}} \right| -\frac{1}{2}; +\frac{\sqrt{3}}{2} \right\rangle \\ &= \overleftrightarrow{A} - \frac{1}{2} \overleftrightarrow{A}_x - \frac{\sqrt{3}}{2} \overleftrightarrow{A}_y.\end{aligned}\quad (\text{D5b})$$

At first glance, $\hat{C}_3 \overleftrightarrow{B}^{(xx)}$ and $\hat{C}_3^{-1} \overleftrightarrow{C}^{(xx)}$ matrices should agree with $A^{(xx)}$ of C_1 . However, the rotation also acts on

the orbitals thus the hyperfine tensor should be evaluated on $|e_{(\pm 120^\circ)}\rangle = \frac{1}{2}|e_x\rangle \pm \frac{\sqrt{3}}{2}|e_y\rangle$ orbitals that we label as $\overleftrightarrow{A}^{(\pm 120^\circ)}$. Eqs. (D4)-(D5a)-(D5b) allow us to determine the orbital flipping matrices directly as

$$\overleftrightarrow{A} = \frac{1}{3} \left(\overleftrightarrow{A}^{(xx)} + \hat{C}_3 \overleftrightarrow{B}^{(xx)} + \hat{C}_3^{-1} \overleftrightarrow{C}^{(xx)} \right), \quad (\text{D6a})$$

$$\overleftrightarrow{A}_x = \frac{q}{4} \left(2 \overleftrightarrow{A}^{(xx)} - \hat{C}_3 \overleftrightarrow{B}^{(xx)} - \hat{C}_3^{-1} \overleftrightarrow{C}^{(xx)} \right), \quad (\text{D6b})$$

$$\overleftrightarrow{A}_y = \frac{q}{\sqrt{3}} \left(\hat{C}_3 \overleftrightarrow{B}^{(xx)} - \hat{C}_3^{-1} \overleftrightarrow{C}^{(xx)} \right), \quad (\text{D6c})$$

where we also included the effect of $q = (1+p)/2$ vibronic reduction factor [56, 57] that partially quenches the strength of $\{\hat{\sigma}_z, \hat{\sigma}_x\}$ orbital operators transforming as E representation of D_{3d} . The p reduction factor reduces the orbital operators transforming as A_2 such as

TABLE XII. The effective dynamic hyperfine parameters for selected ^{13}C nuclear spins in low C_{2h} symmetry for G4V(-) defects as obtained by HSE06 calculations in the electronic ground state. The directions are defined in Fig. 8(e).

Defect	A_{xx} (MHz)	A_{yy} (MHz)	A_{zz} (MHz)	A_{xy} (MHz)	A_{xz} (MHz)	A_{yz} (MHz)
Ground state						
SiV(-) - first neighbor						
A	60.4	43.2	37.5	0.0	7.2	0.0
A_x	-22.0	-6.8	-10.6	-3.0	-4.6	2.7
A_y	-50.7	-15.6	-24.4	2.3	-10.7	-2.1
SiV(-) - second neighbor						
A	-0.6	-2.7	-2.6	-0.8	0.5	-0.3
A_x	0.6	1.1	1.3	0.3	0.1	0.1
A_y	1.8	1.7	2.7	1.0	0.7	-0.6
GeV(-) - first neighbor						
A	77.6	37.0	42.0	0.0	13.9	0.0
A_x	-23.1	-11.5	-13.0	1.2	-4.0	0.4
A_y	-52.9	-26.2	-29.7	-1.0	-9.2	-0.3
GeV(-) - second neighbor						
A	-3.2	-4.3	-4.2	-1.1	-0.2	0.6
A_x	1.7	1.8	2.0	0.4	0.4	-0.4
A_y	1.5	1.9	2.7	0.3	-0.1	0.3
SnV(-) - first neighbor						
A	70.1	28.3	33.4	0.0	14.6	0.0
A_x	-21.4	-9.3	-10.8	1.3	-4.3	0.4
A_y	-49.3	-21.3	-24.9	-1.0	-9.8	-0.3
SnV(-) - second neighbor						
A	-4.1	-5.3	-4.9	-0.8	-0.2	0.5
A_x	1.9	2.1	2.1	0.3	0.4	-0.3
A_y	2.1	2.4	3.2	0.2	-0.1	0.2
PbV(-) - first neighbor						
A	60.4	39.1	33.7	0.0	9.1	0.0
A_x	-26.7	-7.4	-12.2	-4.0	-6.6	3.5
A_y	-61.6	-16.9	-28.1	3.1	-15.2	-2.7
PbV(-) - second neighbor						
A	-4.9	-5.9	-5.2	-0.6	-0.1	0.4
A_x	2.0	2.2	2.1	0.2	0.3	-0.3
A_y	2.9	3.1	3.9	0.1	-0.0	0.1
Excited state						
SiV(-)						
A	15.91	21.81	10.57	-5.13	-2.58	4.46
A_x	1.53	-4.93	0.10	2.09	0.32	-1.73
A_y	-1.10	-6.58	0.30	7.53	2.31	-3.08
GeV(-)						
A	4.80	14.61	1.43	0.94	-3.18	0.44
A_x	4.19	3.52	2.19	6.20	-1.10	-3.53
A_y	4.93	12.90	5.07	-3.26	-1.33	2.83
SnV(-)						
A	54.96	33.86	28.43	0.03	8.83	-0.02
A_x	-18.26	-3.71	-7.19	-2.77	-4.75	2.38
aA_y	-42.01	-8.31	-16.44	2.15	-10.99	-1.85
PbV(-)						
A	27.98	11.04	10.78	0.09	6.77	1.29
A_x	-7.83	0.23	-0.87	1.13	-2.18	0.12
A_y	-19.11	1.60	-2.62	-0.81	-6.72	0.75

$\hat{L}_z = \hat{\sigma}_y$ of Eq. (1). We note that the \overleftrightarrow{A} tensor can be evaluated by putting two half electrons on $|e_x\rangle$ and $|e_y\rangle$

orbitals which method was already used in Ref. 34.

Finally, we list of the electronic hyperfine tensor data in Tables X and XI as obtained in HSE06 calculations that we list for the sake of reproduction of our results

and the derived hyperfine tensor data in Tables XII and III. We note that the hyperfine constants of the second neighbor atoms are almost negligible in the electronic excited state.

-
- [1] V. S. Vavilov and A. Gippius, Investigation of the cathodoluminescence of epitaxial diamond films, *Sov. Phys. Semicond.* **14**, 1078 (1980).
 - [2] C. Hepp, T. Müller, V. Waselowski, J. N. Becker, B. Pingault, H. Sternschulte, D. Steinmüller-Nethl, A. Gali, J. R. Maze, M. Atatüre, and C. Becher, Electronic structure of the silicon vacancy color center in diamond, *Phys. Rev. Lett.* **112**, 036405 (2014).
 - [3] T. Müller, C. Hepp, B. Pingault, E. Neu, S. Gsell, M. Schreck, H. Sternschulte, D. Steinmüller-Nethl, C. Becher, and M. Atatüre, Optical signatures of silicon-vacancy spins in diamond, *Nature Communications* **5**, 3328 (2014).
 - [4] L. J. Rogers, K. D. Jahnke, M. W. Doherty, A. Dietrich, L. P. McGuinness, C. Müller, T. Teraji, H. Sumiya, J. Isoya, N. B. Manson, and F. Jelezko, Electronic structure of the negatively charged silicon-vacancy center in diamond, *Phys. Rev. B* **89**, 235101 (2014).
 - [5] E. A. Ekimov, S. G. Lyapin, K. N. Boldyrev, M. V. Kondrin, R. Khmelnskiy, V. A. Gavva, T. V. Kotereva, and M. N. Popova, Germanium-vacancy color center in isotopically enriched diamonds synthesized at high pressures, *JETP Letters* **102**, 701 (2015).
 - [6] T. Iwasaki, F. Ishibashi, Y. Miyamoto, Y. Doi, S. Kobayashi, T. Miyazaki, K. Tahara, K. D. Jahnke, L. J. Rogers, B. Naydenov, F. Jelezko, S. Yamasaki, S. Nagamachi, T. Inubushi, N. Mizuochi, and M. Hatano, Germanium-vacancy single color centers in diamond, *Scientific Reports* **5**, 12882 (2015).
 - [7] T. Iwasaki, Y. Miyamoto, T. Taniguchi, P. Siyushev, M. H. Metsch, F. Jelezko, and M. Hatano, Tin-vacancy quantum emitters in diamond, *Phys. Rev. Lett.* **119**, 253601 (2017).
 - [8] S. Meesala, Y.-I. Sohn, B. Pingault, L. Shao, H. A. Atikian, J. Holzgrafe, M. Gündoğan, C. Stavarakas, A. Sipahigil, C. Chia, R. Evans, M. J. Burek, M. Zhang, L. Wu, J. L. Pacheco, J. Abraham, E. Bielejec, M. D. Lukin, M. Atatüre, and M. Lončar, Strain engineering of the silicon-vacancy center in diamond, *Phys. Rev. B* **97**, 205444 (2018).
 - [9] S. Ditalia Tchernij, T. Lühmann, T. Herzig, J. Küpper, A. Damin, S. Santonocito, M. Signorile, P. Traina, E. Moreva, F. Celegato, S. Pezzagna, I. P. Degiovanni, P. Olivero, M. Jakšić, J. Meijer, P. M. Genovese, and J. Forneris, Single-photon emitters in lead-implanted single-crystal diamond, *ACS Photonics* **5**, 4864 (2018).
 - [10] M. E. Trusheim, N. H. Wan, K. C. Chen, C. J. Ciccarino, J. Flick, R. Sundararaman, G. Malladi, E. Bersin, M. Walsh, B. Lienhard, H. Bakhru, P. Narang, and D. Englund, Lead-related quantum emitters in diamond, *Phys. Rev. B* **99**, 075430 (2019).
 - [11] D. Chen, N. I. Zheludev, and W. Gao, Building blocks for quantum network based on group-iv split-vacancy centers in diamond, *Advanced Quantum Technologies* **3** (2019).
 - [12] M. E. Trusheim, B. Pingault, N. H. Wan, M. Gündoğan, L. De Santis, R. Debroux, D. Gangloff, C. Purser, K. C. Chen, M. Walsh, J. J. Rose, J. N. Becker, B. Lienhard, E. Bersin, I. Paradeisianos, G. Wang, D. Lyzwa, A. R.-P. Montblanch, G. Malladi, H. Bakhru, A. C. Ferrari, I. A. Walmsley, M. Atatüre, and D. Englund, Transform-limited photons from a coherent tin-vacancy spin in diamond, *Phys. Rev. Lett.* **124**, 023602 (2020).
 - [13] J. Görlitz, D. Herrmann, G. Thiering, P. Fuchs, M. Gandil, T. Iwasaki, T. Taniguchi, M. Kieschnick, J. Meijer, M. Hatano, A. Gali, and C. Becher, Spectroscopic investigations of negatively charged tin-vacancy centres in diamond, *New Journal of Physics* **22**, 013048 (2020).
 - [14] V. S. Krivobok, E. A. Ekimov, S. G. Lyapin, S. N. Nikolaev, Y. A. Skakov, A. A. Razgulo, and M. V. Kondrin, Observation of a 1.979-ev spectral line of a germanium-related color center in microdiamonds and nanodiamonds, *Phys. Rev. B* **101**, 144103 (2020).
 - [15] A. E. Rugar, S. Aghaeimeibodi, D. Riedel, C. Dory, H. Lu, P. J. McQuade, Z.-X. Shen, N. A. Melosh, and J. Vučković, Quantum photonic interface for tin-vacancy centers in diamond, *Phys. Rev. X* **11**, 031021 (2021).
 - [16] S. Aghaeimeibodi, D. Riedel, A. E. Rugar, C. Dory, and J. Vučković, Electrical tuning of tin-vacancy centers in diamond, *Phys. Rev. Appl.* **15**, 064010 (2021).
 - [17] P. Wang, T. Taniguchi, Y. Miyamoto, M. Hatano, and T. Iwasaki, Low-temperature spectroscopic investigation of lead-vacancy centers in diamond fabricated by high-pressure and high-temperature treatment, *ACS Photonics* **8**, 2947 (2021).
 - [18] B. Vindole, M.-P. Adam, L. Toraille, M. Chipaux, A. Hilberer, G. Dupuy, L. Razinkovas, A. Alkauskas, G. Thiering, A. Gali, M. De Feudis, M. W. Ngandeu Ngambou, J. Achard, A. Tallaire, M. Schmidt, C. Becher, and J.-F. Roch, Optical properties of siv and gev color centers in nanodiamonds under hydrostatic pressures up to 180 gpa, *Phys. Rev. B* **106**, 214109 (2022).
 - [19] P. Wang, L. Kazak, K. Senkalla, P. Siyushev, R. Abe, T. Taniguchi, S. Onoda, H. Kato, T. Makino, M. Hatano, F. Jelezko, and T. Iwasaki, Transform-limited photon emission from a lead-vacancy center in diamond above 10 k, *Phys. Rev. Lett.* **132**, 073601 (2024).
 - [20] M. K. Bhaskar, R. Riedinger, B. Machielse, D. S. Levonian, C. T. Nguyen, E. N. Knall, H. Park, D. Englund, M. Lončar, D. D. Sukachev, and M. D. Lukin, Experimental demonstration of memory-enhanced quantum communication, *Nature* **580**, 60 (2020).
 - [21] E. Bersin, M. Sutula, Y. Q. Huan, A. Suleymanzade, D. R. Assumpcao, Y.-C. Wei, P.-J. Stas, C. M. Knaut, E. N. Knall, C. Langrock, N. Sinclair, R. Murphy, R. Riedinger, M. Yeh, C. Xin, S. Bandyopadhyay, D. D. Sukachev, B. Machielse, D. S. Levonian, M. K. Bhaskar, S. Hamilton, H. Park, M. Lončar, M. M. Fejer, P. B. Dixon, D. R. Englund, and M. D. Lukin, Telecom net-

- working with a diamond quantum memory, *PRX Quantum* **5**, 010303 (2024).
- [22] C. M. Knaut, A. Suleymanzade, Y.-C. Wei, D. R. Assumpcao, P.-J. Stas, Y. Q. Huan, B. Machielse, E. N. Knall, M. Sutula, G. Baranes, N. Sinclair, C. De-Eknamkul, D. S. Levonian, M. K. Bhaskar, H. Park, M. Lončar, and M. D. Lukin, Entanglement of nanophotonic quantum memory nodes in a telecom network, *Nature* **629**, 573 (2024).
 - [23] J. P. Goss, R. Jones, S. J. Breuer, P. R. Briddon, and S. Öberg, The twelve-line 1.682 eV luminescence center in diamond and the vacancy-silicon complex, *Phys. Rev. Lett.* **77**, 3041 (1996).
 - [24] A. Gali and J. R. Maze, Ab initio study of the split silicon-vacancy defect in diamond: Electronic structure and related properties, *Phys. Rev. B* **88**, 235205 (2013).
 - [25] G. Thiering and A. Gali, Ab initio magneto-optical spectrum of group-IV vacancy color centers in diamond, *Phys. Rev. X* **8**, 021063 (2018).
 - [26] M. W. Doherty, N. B. Manson, P. Delaney, F. Jelezko, J. Wrachtrup, and L. C. Hollenberg, The nitrogen-vacancy colour centre in diamond, *Physics Reports* **528**, 1 (2013).
 - [27] A. Gali, Ab initio theory of the nitrogen-vacancy center in diamond, *Nanophotonics* **8**, 1907 (2019).
 - [28] B. Pingault, J. N. Becker, C. H. H. Schulte, C. Arend, C. Hepp, T. Godde, A. I. Tartakovskii, M. Markham, C. Becher, and M. Atatüre, All-optical formation of coherent dark states of silicon-vacancy spins in diamond, *Phys. Rev. Lett.* **113**, 263601 (2014).
 - [29] J. N. Becker, J. Görlitz, C. Arend, M. Markham, and C. Becher, Ultrafast all-optical coherent control of single silicon vacancy colour centres in diamond, *Nature Communications* **7**, 13512 (2016).
 - [30] P. Siyushev, M. H. Metsch, A. Ijaz, J. M. Binder, M. K. Bhaskar, D. D. Sukachev, A. Sipahigil, R. E. Evans, C. T. Nguyen, M. D. Lukin, P. R. Hemmer, Y. N. Palyanov, I. N. Kupriyanov, Y. M. Borzdov, L. J. Rogers, and F. Jelezko, Optical and microwave control of germanium-vacancy center spins in diamond, *Phys. Rev. B* **96**, 081201 (2017).
 - [31] J. N. Becker, B. Pingault, D. Groß, M. Gündoğan, N. Kukharchyk, M. Markham, A. Edmonds, M. Atatüre, P. Bushev, and C. Becher, All-optical control of the silicon-vacancy spin in diamond at millikelvin temperatures, *Phys. Rev. Lett.* **120**, 053603 (2018).
 - [32] C. Weinzetl, J. Görlitz, J. N. Becker, I. A. Walmsley, E. Poem, J. Nunn, and C. Becher, Coherent control and wave mixing in an ensemble of silicon-vacancy centers in diamond, *Phys. Rev. Lett.* **122**, 063601 (2019).
 - [33] R. Debroux, C. P. Michaels, C. M. Purser, N. Wan, M. E. Trusheim, J. Arjona Martínez, R. A. Parker, A. M. Stramma, K. C. Chen, L. de Santis, E. M. Alexeev, A. C. Ferrari, D. Englund, D. A. Gangloff, and M. Atatüre, Quantum control of the tin-vacancy spin qubit in diamond, *Phys. Rev. X* **11**, 041041 (2021).
 - [34] I. B. Harris, C. P. Michaels, K. C. Chen, R. A. Parker, M. Titze, J. Arjona Martínez, M. Sutula, I. R. Christen, A. M. Stramma, W. Roth, C. M. Purser, M. H. Appel, C. Li, M. E. Trusheim, N. L. Palmer, M. L. Markham, E. S. Bielejec, M. Atatüre, and D. Englund, Hyperfine spectroscopy of isotopically engineered group-IV color centers in diamond, *PRX Quantum* **4**, 040301 (2023).
 - [35] S. L. Altmann and P. Herzog, *Point-Group Theory Tables* (Clarendon Press ; Oxford University Press, Oxford : New York, 1994).
 - [36] W. Kohn and L. J. Sham, Self-consistent equations including exchange and correlation effects, *Phys. Rev.* **140**, A1133 (1965).
 - [37] P. Hohenberg and W. Kohn, Inhomogeneous electron gas, *Phys. Rev.* **136**, B864 (1964).
 - [38] P. E. Blöchl, Projector augmented-wave method, *Phys. Rev. B* **50**, 17953 (1994).
 - [39] G. Kresse and D. Joubert, From ultrasoft pseudopotentials to the projector augmented-wave method, *Phys. Rev. B* **59**, 1758 (1999).
 - [40] G. Kresse and J. Furthmüller, Efficient iterative schemes for ab initio total-energy calculations using a plane-wave basis set, *Phys. Rev. B* **54**, 11169 (1996).
 - [41] G. Kresse and J. Furthmüller, Efficiency of ab-initio total energy calculations for metals and semiconductors using a plane-wave basis set, *Computational Materials Science* **6**, 15 (1996).
 - [42] J. Sun, A. Ruzsinszky, and J. P. Perdew, Strongly constrained and appropriately normed semilocal density functional, *Phys. Rev. Lett.* **115**, 036402 (2015).
 - [43] E. B. Isaacs and C. Wolverton, Performance of the strongly constrained and appropriately normed density functional for solid-state materials, *Phys. Rev. Mater.* **2**, 063801 (2018).
 - [44] D. Mejia-Rodriguez and S. B. Trickey, Deorbitalized meta-gga exchange-correlation functionals in solids, *Phys. Rev. B* **98**, 115161 (2018).
 - [45] M. Maciaszek, V. Žalandauskas, R. Silkinis, A. Alkauskas, and L. Razinkovas, The application of the SCAN density functional to color centers in diamond, *J. Chem. Phys.* **159**, 084708 (2023).
 - [46] J. Heyd, G. E. Scuseria, and M. Ernzerhof, Hybrid functionals based on a screened coulomb potential, *The Journal of Chemical Physics* **118**, 8207 (2003).
 - [47] A. Gali, Theory of the neutral nitrogen-vacancy center in diamond and its application to the realization of a qubit, *Phys. Rev. B* **79**, 235210 (2009).
 - [48] E. U. Condon and G. H. Shortley, *The theory of atomic spectra* (Cambridge University Press, Cambridge, UK ;, 1935).
 - [49] See Supplemental Material of Ref. [2].
 - [50] S. Häußler, G. Thiering, A. Dietrich, N. Waasem, T. Teraji, J. Isoya, T. Iwasaki, M. Hatano, F. Jelezko, A. Gali, and A. Kubanek, Photoluminescence excitation spectroscopy of SiV- and GeV-color center in diamond, *New Journal of Physics* **19**, 063036 (2017).
 - [51] F. S. Ham, Dynamical Jahn-Teller effect in paramagnetic resonance spectra: Orbital reduction factors and partial quenching of spin-orbit interaction, *Phys. Rev.* **138**, A1727 (1965).
 - [52] P. E. Blöchl, First-principles calculations of defects in oxygen-deficient silica exposed to hydrogen, *Phys. Rev. B* **62**, 6158 (2000).
 - [53] K. Szász, T. Hornos, M. Marsman, and A. Gali, Hyperfine coupling of point defects in semiconductors by hybrid density functional calculations: The role of core spin polarization, *Phys. Rev. B* **88**, 075202 (2013).
 - [54] See Supplemental Material of Ref. [67].
 - [55] F. S. Ham, Effect of Linear Jahn-Teller Coupling on Paramagnetic Resonance in a E_2 State, *Physical Review* **166**, 1008 (1968).

- 307 (1968).
- [56] I. B. Bersuker, *The Jahn-Teller effect* (Cambridge University Press, Cambridge, UK, 2006).
 - [57] I. Bersuker and V. Polinger, *Vibronic Interactions in Molecules and Crystals*, Springer Series in Chemical Physics (Springer Berlin Heidelberg, 2012).
 - [58] S. Steiner, S. Khmelevskyi, M. Marsmann, and G. Kresse, Calculation of the magnetic anisotropy with projected-augmented-wave methodology and the case study of disordered $\text{Fe}_{1-x}\text{Co}_x$ alloys, *Phys. Rev. B* **93**, 224425 (2016).
 - [59] R. Bruyndonckx, C. Daul, P. T. Manoharan, and E. Deiss, A nonempirical approach to ground-state jahn-teller distortion: Case study of VCl_4 , *Inorganic Chemistry* **36**, 4251 (1997).
 - [60] P. Deák, B. Aradi, T. Frauenheim, E. Janzén, and A. Gali, Accurate defect levels obtained from the hse06 range-separated hybrid functional, *Phys. Rev. B* **81**, 153203 (2010).
 - [61] C. Freysoldt, B. Grabowski, T. Hickel, J. Neugebauer, G. Kresse, A. Janotti, and C. G. Van de Walle, First-principles calculations for point defects in solids, *Rev. Mod. Phys.* **86**, 253 (2014).
 - [62] A. Csóré, I. G. Ivanov, N. T. Son, and A. Gali, Fluorescence spectrum and charge state control of divacancy qubits via illumination at elevated temperatures in 4h silicon carbide, *Phys. Rev. B* **105**, 165108 (2022).
 - [63] G. Thiering and A. Gali, Ab initio calculation of spin-orbit coupling for an nv center in diamond exhibiting dynamic jahn-teller effect, *Phys. Rev. B* **96**, 081115 (2017).
 - [64] B. L. Green, S. Mottishaw, B. G. Breeze, A. M. Edmonds, U. F. S. D’Haenens-Johansson, M. W. Doherty, S. D. Williams, D. J. Twitchen, and M. E. Newton, Neutral silicon-vacancy center in diamond: Spin polarization and lifetimes, *Phys. Rev. Lett.* **119**, 096402 (2017).
 - [65] M. H. Metsch, K. Senkalla, B. Tratzmiller, J. Scheuer, M. Kern, J. Achard, A. Tallaie, M. B. Plenio, P. Siyushev, and F. Jelezko, Initialization and readout of nuclear spins via a negatively charged silicon-vacancy center in diamond, *Phys. Rev. Lett.* **122**, 190503 (2019).
 - [66] R. Monge, T. Delord, G. Thiering, A. Gali, and C. A. Meriles, Resonant versus nonresonant spin readout of a nitrogen-vacancy center in diamond under cryogenic conditions, *Phys. Rev. Lett.* **131**, 236901 (2023).
 - [67] G. Thiering and A. Gali, Nuclear spin relaxation in solid-state-defect quantum bits via electron-phonon coupling in the optical excited state, *Phys. Rev. Appl.*, (2025).
 - [68] K. V. Kepesidis, M.-A. Lemonde, A. Norambuena, J. R. Maze, and P. Rabl, Cooling phonons with phonons: Acoustic reservoir engineering with silicon-vacancy centers in diamond, *Phys. Rev. B* **94**, 214115 (2016).
 - [69] L. J. Rogers, K. D. Jahnke, M. H. Metsch, A. Sipahigil, J. M. Binder, T. Teraji, H. Sumiya, J. Isoya, M. D. Lukin, P. Hemmer, and F. Jelezko, All-optical initialization, readout, and coherent preparation of single silicon-vacancy spins in diamond, *Phys. Rev. Lett.* **113**, 263602 (2014).
 - [70] M. Haouas, F. Taulelle, and C. Martineau, Recent advances in application of ^{27}Al nmr spectroscopy to materials science, *Progress in Nuclear Magnetic Resonance Spectroscopy* **94-95**, 11 (2016).
 - [71] P. Pykkö, Year-2008 nuclear quadrupole moments, *Molecular Physics* **106**, 1965 (2008), <https://doi.org/10.1080/00268970802018367>.
 - [72] G. m. H. Thiering and A. Gali, Erratum: Ab initio magneto-optical spectrum of group-iv vacancy color centers in diamond [phys. rev. x 8, 021063 (2018)], *Phys. Rev. X* **10**, 039901 (2020).
 - [73] K. W. H. Stevens, On the magnetic properties of covalent xy 6 complexes, *Proceedings of the Royal Society of London A: Mathematical, Physical and Engineering Sciences* **219**, 542 (1953).
 - [74] A. E. Rugar, C. Dory, S. Sun, and J. Vučković, Characterization of optical and spin properties of single tin-vacancy centers in diamond nanopillars, *Phys. Rev. B* **99**, 205417 (2019).
 - [75] K. D. Jahnke, A. Sipahigil, J. M. Binder, M. W. Doherty, M. Metsch, L. J. Rogers, N. B. Manson, M. D. Lukin, and F. Jelezko, Electron-phonon processes of the silicon-vacancy centre in diamond, *New Journal of Physics* **17**, 043011 (2015).
 - [76] G. Thiering and A. Gali, Magneto-optical spectra of the split nickel-vacancy defect in diamond, *Phys. Rev. Res.* **3**, 043052 (2021).
 - [77] B. Pingault, D.-D. Jarausch, C. Hepp, L. Klintberg, J. N. Becker, M. Markham, C. Becher, and M. Atatüre, Coherent control of the silicon-vacancy spin in diamond, *Nature Communications* **8**, 15579 (2017).
 - [78] D. D. Sukachev, A. Sipahigil, C. T. Nguyen, M. K. Bhaskar, R. E. Evans, F. Jelezko, and M. D. Lukin, Silicon-vacancy spin qubit in diamond: A quantum memory exceeding 10 ms with single-shot state readout, *Phys. Rev. Lett.* **119**, 223602 (2017).
 - [79] K. Senkalla, G. Genov, M. H. Metsch, P. Siyushev, and F. Jelezko, Germanium vacancy in diamond quantum memory exceeding 20 ms, *Phys. Rev. Lett.* **132**, 026901 (2024).
 - [80] M. W. Doherty, V. V. Struzhkin, D. A. Simpson, L. P. McGuinness, Y. Meng, A. Stacey, T. J. Karle, R. J. Hemley, N. B. Manson, L. C. L. Hollenberg, and S. Prawer, Electronic properties and metrology applications of the diamond nv^- center under pressure, *Phys. Rev. Lett.* **112**, 047601 (2014).
 - [81] A. Hilberer, L. Toraille, C. Dailledouze, M.-P. Adam, L. Hanlon, G. Weck, M. Schmidt, P. Loubeyre, and J.-F. m. c. Roch, Enabling quantum sensing under extreme pressure: Nitrogen-vacancy magnetometry up to 130 gpa, *Phys. Rev. B* **107**, L220102 (2023).
 - [82] K. O. Ho, K. C. Wong, M. Y. Leung, Y. Y. Pang, W. K. Leung, K. Y. Yip, W. Zhang, J. Xie, S. K. Goh, and S. Yang, Recent developments of quantum sensing under pressurized environment using the nitrogen vacancy (nv) center in diamond, *Journal of Applied Physics* **129**, 241101 (2021), <https://pubs.aip.org/aip/jap/article-pdf/doi/10.1063/5.0052233/19891745/241101.1.5.0052233.pdf>.
 - [83] Data supporting “Additional data for the effective spin-orbit splitting of G4V centers in diamond”, Available from the corresponding author upon reasonable request. Correspondence: gali.adam@wigner.hun-ren.hu (2025).
 - [84] C. Freysoldt, J. Neugebauer, and C. G. Van de Walle, Fully ab initio finite-size corrections for charged-defect supercell calculations, *Phys. Rev. Lett.* **102**, 016402 (2009).
 - [85] C. Freysoldt, J. Neugebauer, and C. G. Van de Walle, Electrostatic interactions between charged defects in supercells, *physica status solidi (b)* **248**, 1067 (2011), <https://onlinelibrary.wiley.com/doi/pdf/10.1002/pspb.201046289>.

- [86] M. Gajdoš, K. Hummer, G. Kresse, J. Furthmüller, and F. Bechstedt, Linear optical properties in the projector-augmented wave methodology, *Phys. Rev. B* **73**, 045112 (2006).
- [87] S. Baroni and R. Resta, Ab initio calculation of the macroscopic dielectric constant in silicon, *Phys. Rev. B* **33**, 7017 (1986).
- [88] J. P. Elliott and P. G. Dawber, *Symmetry in Physics Vol1* (Macmillan Education UK, London, 1979).